Receptivity of a transitional shock/boundary-layer interaction to shock oscillations in hypersonic flow

CERMINARA, Adriano, LEVIN, Deborah and THEOFILIS, Vassilis

This document is the Accepted Version [AM]

Citation:

CERMINARA, Adriano, LEVIN, Deborah and THEOFILIS, Vassilis (2026). Receptivity of a transitional shock/boundary-layer interaction to shock oscillations in hypersonic flow. AIAA Journal. [Article]

Receptivity of a transitional shock/boundary-layer interaction to shock oscillations in hypersonic flow

Adriano Cerminara [*]
Sheffield Hallam University, Sheffield S1 1WB, UK

Deborah Levin [†]
University of Illinois at Urbana-Champaign, 104 S. Wright St. Urbana, IL 61801-2935, United States

Vassilis Theofilis [‡]
Technion - Israel Institute of Technology, Haifa 32000, Israel

The present work studies the complex dynamics of an oscillating shock impinging on a laminar/transitional supersonic boundary layer, with emphasis on the radiated post-shock waves and a coherent wave structure induced in the turbulent boundary layer (TBL) downstream of the separation bubble. Fully-resolved Direct Numerical Simulations (DNS) have been carried out at Mach 5, with imposed shock-oscillation frequency matching that predicted by earlier Direct Simulation Monte Carlo (DSMC) studies of the internal shock structure. Shock oscillations are found to produce a field of post-shock waves efficiently transmitted through the reattachment shock into the downstream TBL. The flow response consists of two-dimensional amplified planar waves propagating downstream with sustained amplitude. Increasing shock-oscillation amplitudes progressively enhance this phenomenon, while increasing frequencies, within the DSMC-predicted range, are found to promote a greater disturbance amplification, with amplitudes larger by 50 % compared to lower frequencies. This indicates a high susceptibility of the wave transmission mechanism to the shock-oscillation frequencies. Conversely, the region between separation and reattachment shock is found to be sensitive to frequencies different from those of the shock oscillations. This previously unknown generation mechanism of a 2D planar wave system within the TBL is altogether absent when the impinging shock is steady.

Nomenclature

C = ratio of Sutherland's constant to reference temperature

---

[*] Senior Lecturer in Aerospace Engineering, School of Engineering and Built Environment, a.cerminara@shu.ac.uk, AIAA Member (Corresponding Author)

[†] Professor of Aerospace Engineering, AIAA Fellow

[‡] Professor of Aerospace Engineering, Faculty of Aerospace Engineering, AIAA Associate Fellow

Presented at AIAA SciTech Forum, 8-12 January, 2024, Orlando (FL), AIAA Pap. 2024-0290

c_p, c_v = specific heats at constant pressure and volume

E = total energy

$\boldsymbol{F}$ = flux vector

f = frequency

L = computational domain length in a given direction

M = Mach number

N = number of grid points in a given direction

Pr = Prandtl number

p = static pressure

$\boldsymbol{Q}$ = vector of the conservative variables

Re = Reynolds number

T = static temperature

t = time

U = magnitude of the velocity vector

u, v, w = velocity components

x, y, z = Cartesian coordinates in the streamwise, wall-normal and spanwise direction, respectively

δ = boundary-layer displacement thickness

γ = ratio of the specific heats

λ = wavelength

μ = dynamic viscosity

ρ = density

τ = viscous stresses

Subscripts

i, j, k = indices of grid-line directions in the streamwise, wall-normal and spanwise direction, respectively

x, y, z = directions in the Cartesian reference system

w = at the wall

∞ = freestream quantity

Superscripts

$*$ = dimensional quantity

I. Introduction

Transition to turbulence plays a crucial role on the heat-transfer rates on the surface of hypersonic vehicles, which makes it necessary to understand the physical mechanism responsible for transition, in order to allow accurate prediction of the transition location. The shock/boundary-layer-interaction (SBLI) phenomenon is among the most relevant mechanism that produces a dramatic increase of the aerodynamic heating, in combination with highly unsteady flow, as well as other important consequences terms of vehicle stability and control. The size of the separation bubble is highly dependent on the shock intensity and on the boundary-layer state [1, 2]. The separation length was found to be linearly dependent on the shock intensity in the experiments of Hakkinen et al. [3] and the numerical simulations of Katzer [4]. Lusher and Sandham [5] numerically studied the effects of flow confinement on a laminar SBLI, and found that both duct aspect ratio and the expansion fan at the trailing edge of the shock generator highly affect the interaction. Babinsky and Harvey [6] found that the separation in SBLI is highly dependent on the state of the upstream boundary layer. While the flow characteristics of laminar SBLI have been studied extensively and are well established in the literature, the case of SBLI in transitional and turbulent boundary layers have not been fully understood yet. A numerical study of Sivasubramanian and Fasel [7] showed that disturbances in the upstream boundary layer are strongly amplified by the laminar separation bubble, with transition to turbulence occurring at larger shock intensities. In the work of Sansica et al. [8], the introduction of unstable oblique modes in a laminar SBLI led to transition to turbulence downstream of the reattachement point. The DNS study of Dwivedi et al. [9] at Mach 5.92 in laminar flow found a strong disturbance growth downstream of the reattachment point, in combination with unsteadiness and flow three-dimensionalisation at sufficiently high intensities of the incident shock. The work of Sandham et al. [10] provided an assessment of the characteristics of transitional shock/boundary-layer interactions at Mach 6. The authors found that the transition process, at the considered flow conditions, develops from second (Mack) instabilities superimposed on streamwise streaks, and that the Stanton number overshoots are larger for transitional interactions than the case of fully turbulent interaction.

Boundary-layer receptivity concerns the study of how the boundary layer internalizes the impinging disturbances from the upstream flow, in the form of internal instability modes. In this context, the body leading edge is a highly-receptive zone, due to the non-parallel effects and the related short-scale streamwise variations of the mean flow, which, in turn, cause a wavelength-conversion process from the scale of the external forcing to that of the induced boundary-layer disturbances [11]. At hypersonic Mach numbers, however, it is well known that the small differences in phase speed between forcing waves and boundary-layer dominant modes lead to a direct excitation of these modes via a resonance mechanism at the leading edge [12, 13], without the need of a wavelength-conversion mechanism. Several numerical studies on the role of different types of freestream disturbances, particularly fast and slow acoustic waves, in the above-mentioned resonance mechanism, have been carried out [14–22], which highlighted the complex wave interaction features of the leading-edge receptivity, the synchronisation with the external forcing, downstream modulation and evolution of different induced boundary-layer modes, whose type and relative significance in the transition process depend on the types and characteristics of the external impinging disturbances.

However, another receptive region of the flow is represented by the shock, whose susceptibility to external and wall-reflected waves, as well as to inner molecular collisions, is a source of additional wave modes, which propagate within the shock layer, i.e. the flow region between the shock and the solid surface, and impinge onto the boundary layer modulating the whole receptivity process. In shock/boundary-layer interaction cases, the presence of an oscillating shock can significantly affect the flow features in the interaction region and in the downstream boundary layer. This might produce disturbances in key quantities, such as wall pressure, temperature, skin friction and surface heat flux, which can compromise the vehicle structural integrity and adversely impact on the aerodynamics, flight dynamics and propulsion performance. Most of the literature on the unsteadiness of shock/boundary-layer interactions has focused on explaining the mechanism behind the low-frequency large-scale oscillations of the reflected shock which is associated with frequencies of one or two order of magnitudes lower than the characteristic frequencies of the incoming turbulent boundary layer [23]. Several experimental and numerical studies dedicated to the SBLI unsteadiness phenomenon led to a differentiation between two main mechanisms, namely an 'upstream' mechanism which correlates the SBLI unsteadiness to flow features or events in the upstream turbulent boundary layer (see e.g. [24, 25]), and a 'downstream' mechanism in which the source of unsteadiness is correlated to events occurring downstream of the reattachment shock. The latter includes sources such as fluid entrainment due to the shear layer downstream of the reflected shock and feedback into the separation bubble[26, 27], or acoustic feedback due to acoustic waves generated in the downstream shear-layer and propagating upstream within the separation bubble [28, 29].

Both types of 'upstream' and 'downstream' mechanisms are associated with events within the boundary-layer and shear-layer flows either upstream or downstream of the interaction region. However, not much attention has been devoted to the oscillations of the shock due to different sources. Unsteadiness of the SBLI can, in fact, be induced by other mechanisms, such as freestream waves (e.g. acoustic and vortical waves, or entropy spottiness) interacting with and producing oscillations of the impinging shock, as well as structural vibrations and change of the flight conditions, which can cause large-scale fluctuations of the impinging shock and the entire SBLI shock system. Recent literature has focused on the fluid-structure interaction in SBLI cases with shocks impinging on flexible surfaces and the role of the shock-generator motion [30–34]. The considered frequencies for the motion of the shock generator reflect a low-frequency range, i.e. $f \approx 10 - 100$ Hz, corresponding to typical frequencies associated with changes of flow conditions due to e.g. vehicle maneuvers, control surfaces and aeroelastic interaction [34]. For example, Miller et al. [33] considered a frequency of 10 Hz for the oscillating incident shock in their computational fluid-thermal-structural model, whereas Currao et al. [34] imposed pitch oscillations of the shock generator with a frequency of 42 Hz in their combined experimental-numerical study. The order of these frequencies is, however, significantly different to the order of the relevant frequency range associated with freestream disturbances, e.g. acoustic noise, vorticity and entropy waves. The broadband noise environment of hypersonic wind tunnels is characterized by significant disturbance amplitudes within a frequency range on the order of several tens to hundreds of kilohertz, i.e. $\mathcal{O}(10-10^2)$ kHz [35]. In the combined experimental-numerical study of Wagner et al. [35], for example, which was one of the first studies dedicated to the identification of the noise levels in the environment of different hypersonic ground-test facilities at DLR, larger signal amplitudes were found for frequencies below 50 kHz in RWG and below 100 kHz in HLB for lower unit Reynolds numbers, and for higher frequencies (above 100 kHz) at larger unit Reynolds numbers. These, in turn, represent frequencies relevant to the boundary-layer receptivity and wave instabilities. The response of incident shock waves in the higher frequency range typical of freestream disturbances, and the resulting effects on the SBLI dynamics, has received limited attention in the existing literature.

Furthermore, recent studies have demonstrated that shock waves can exhibit self-induced oscillations through internal mechanisms associated with thermal non-equilibrium and molecular interactions within the shock structure [36–38]. This phenomenon is referred to here as ‘natural’ shock oscillations. In contrast, oscillations arising from interactions with freestream disturbances can be generally classified as a form of ‘forced’ shock oscillations. Interestingly, the frequencies associated with ‘natural’ shock oscillations fall within the range typical of environmental noise. In their DSMC simulations, for instance, Sawant et al. [37] observed a linear increase in oscillation frequency from approximately 12 kHz to 37 kHz as the Mach number increased from 3 to 10. In particular, the authors [36–38] demonstrated the correlation between the formation of oscillations inside the shock layer and the shock bimodality. The latter is a phenomenon correlated to molecular interactions and represented by a Mach-dependent bimodal shape of the probability density function (PDF) of the energy of particles inside the shock, which has been found to have the form of a non-central chi-squared (NCCS) distribution [37]. Within the shock, the PDF peaks at two different energy values, corresponding to collisions between molecules upstream and downstream of the shock. These in turn will cause waves that are transmitted from the shock into the downstream (post-shock) flow field. This phenomenon is inaccessible to continuum description and the Navier-Stokes equations of motion. This type of additional forcing due to kinetic fluctuations of the shock belongs to the category of “stochastic forcing”, emphasised by Fedorov and Tumin [39] as responsible for the generation of unstable boundary-layer modes which undergo a significant amplification toward the nonlinear region and can lead to transition to turbulence. This behaviour was observed in DSMC studies of Tumuklu et al. [40] for the case of oblique shocks over a double cone. Sawant et al.’s [36–38] work has very recently been extended by combining DSMC to data-driven methods, namely spectral proper orthogonal decomposition (SPOD) and direct mode decomposition (DMD), to identify spatio-temporal coherent structures in DSMC unsteady flows [41]. In particular, Karpuzcu et al. [41] have considered the unsteadiness of the shock layer downstream of oblique shocks over compression-expansion ramp geometries.

Oscillations emitted by the shock within the DSMC-predicted frequency range [37] can, in turn, propagate through the shock layer and interact with the boundary layer, potentially inducing additional flow instabilities. Whilst the classic literature on hypersonic receptivity and transition has always focused on the role of either freestream disturbances or local perturbations on the surface, as well as leading-edge effects, the role of the shock as an active source of instability modes has never been properly addressed. This, in turn, warrants careful attention, as the characteristics of the transition mechanism as well as the transitional and turbulent boundary layer may depend on the nature of disturbances radiated into the post-shock region by an oscillating shock. In the DNS of Cerminara and Sandham [42] for a flow over a swept wedge, for example, a previously unseen transition mechanism has been found, which is associated with the generation at the leading edge and downstream growth of a high-spanwise wavenumber mode, whose source has been found correlated with a shock-wall wave reflection mechanism. This demonstrates that oscillations radiated from the shock can induce early transition in hypersonic flow. Moreover, in the study of Klothakis et al. [43], induced shock oscillations in DSMC simulations have been found synchronized with boundary layer disturbances analysed through linear stability analysis (LST). More recently, the work of Cerminara, Levin and Theofilis [44] showed how shock oscillations at the DSMC-predicted frequencies cause generation of post-shock waves in the shock layer and consequent formation of additional boundary-layer modes, including high-frequency modes, in a range of Mach numbers. This is in line with the work of Sawant et al. [36] for the linear three-dimensional instability of a shock wave / boundary layer interaction in a Mach 7 flow over a double wedge, where a spanwise periodic instability mode was found within the internal structure of the shock layer and the separation bubble.

In light of this, there is a need to explore the unsteadiness of oscillating shock/boundary-layer interaction flows in a higher frequency range typical of e.g. freestream disturbances as well as self-induced (‘natural’) shock oscillations. For this reason, the present study aims at the analysis, via DNS, of the receptivity of a transitional shock/boundary-layer interaction to oscillations of the incident shock, specifically within the DSMC-predicted frequency range [37], which is relevant, as described above, for both cases of ‘forced’ (e.g. environmental) and ‘natural’ (self-induced) shock oscillations. The receptivity of the shock layer and the susceptibility of the downstream turbulent boundary layer to the shock oscillations is analysed in detail, considering different frequencies and amplitudes of the incident shock oscillations, which provides fundamental insights in the complex dynamics of the interaction between an oscillating shock and a transitional boundary layer. It is important to mention that our simulations do not resolve the ‘natural’ (self-induced) shock oscillations, since the thermal non-equilibrium internal to the shock is a phenomenon inaccessible the Navier-Stokes equations of motion. In contrast, our simulations are intended to mimic an oscillatory motion of the shock generator at imposed frequencies (by means of an appropriate time-dependent boundary condition) similar to those observed by Sawant et al.[37], with the aim to investigate the associated receptivity patterns of the transitional shock/boundary-layer interaction phenomenon.

II. Numerical method

A. Governing equations

We consider numerical solutions of the three-dimensional Navier-Stokes equations for compressible flows, written in conservation form, under the assumption of perfect gas. The set of non-dimensional conservation equations in Cartesian coordinates can be written as

$$\frac{\partial \mathbf{Q}}{\partial t} + \frac{\partial (\mathbf{F}_j)}{\partial x_j} = 0 \,, \tag{1}$$

In the equation above, $\mathbf{Q}$ is the vector of the conservative variables, while $\mathbf{F}_j$ is the vector of the fluxes in Cartesian coordinates. The components of the vectors of the system in conservative form are

$$\mathbf{Q} = \begin{bmatrix} \rho \\ \rho u \\ \rho v \\ \rho w \\ \rho E \end{bmatrix} , \tag{2}$$

$$\mathbf{F}_j = \begin{bmatrix} \rho u_j \\ \rho u u_j + \delta_{1j} p - \frac{1}{Re} \tau_{1j} \\ \rho v u_j + \delta_{2j} p - \frac{1}{Re} \tau_{2j} \\ \rho w u_j + \delta_{3j} p - \frac{1}{Re} \tau_{3j} \\ \rho \left(E + \frac{p}{\rho} \right) u_j - \frac{1}{Re} \left(u \tau_{1j} + v \tau_{2j} + w \tau_{3j} + \frac{\mu}{(\gamma - 1) Pr M^2} \frac{\partial T}{\partial x_j} \right) \end{bmatrix} . \tag{3}$$

The terms ρ, ρu, ρv, ρw and ρE are the conservative variables of the system of equations, where ρ is the density, u, v and w are the velocity components respectively in the x, y and z directions, and E is the total energy per unit mass. In the flux vectors, the terms p, T, τ_{ij}, and μ are respectively the pressure, the temperature, the components of the viscous stress tensor, and the dynamic viscosity of the flow, whereas δ_{ij} is the Kronecker delta function. The boundary-layer displacement thickness at the inflow boundary (δ^*) is chosen as the characteristic length to normalise the length scales, while the time scales are normalised with respect to the fluid dynamic characteristic time (δ^*/U^*_∞), based on the velocity of the undisturbed flow and on the characteristic length. The Reynolds number is defined with respect to the boundary-layer displacement thickness at the inlet, as $Re = (\rho^*_\infty U^*_\infty \delta^*)/\mu^*_\infty$; the Prandtl number is set to 0.72 for air, and γ is equal to 1.4, as we are considering a perfect gas model. The dynamic viscosity is, in turn, expressed in terms of temperature by Sutherland's law

$$\mu = T^{3/2}\frac{1+C}{T+C} \,, \tag{4}$$

where the constant C represents the ratio between the Sutherland's constant (set to 110.4 K) and the reference temperature (T^*_∞). The viscous stresses are defined in terms of the velocity derivatives, under the assumption of a Newtonian fluid, as

$$\tau_{ij} = \mu\left[\frac{\partial u_i}{\partial x_j} + \frac{\partial u_j}{\partial x_i} - \frac{2}{3}\delta_{ij}\frac{\partial u_k}{\partial x_k}\right] . \tag{5}$$

We also need a relation linking the total energy to the temperature, which in non-dimensional form can be expressed as

$$E = \frac{T}{\gamma(\gamma-1)M^2} + \frac{1}{2}\left(u^2 + v^2 + w^2\right) \, . \tag{6}$$

Finally, the system of equations is closed by the equation of state for a perfect gas

$$p = \frac{1}{\gamma M^2}\rho T \, . \tag{7}$$

The code used to carry out the numerical simulations is SBLI (Shock-Boundary-Layer-Interaction), developed over a number of years at the University of Southampton, consisting of a 4^{th}-order central differencing scheme, as the base scheme, in conjunction with a 2^{nd}-order Harten-Yee TVD (Total-Variation-Diminishing) shock-capturing scheme [45], as a filter step. The validation of the code can be found in De Tullio *et al.*[46].

III. Computational domain and simulation settings

A. Flow and boundary conditions

A rectangular-box computational domain for a flat plate is considered, with dimensionless size $L_x = 300$, $L_y = 30$, and $L_z = 48$, along the streamwise, wall-normal and spanwise directions, respectively. The inflow conditions of the present study are based on previous studies [47, 48] for Mach 5 wind-tunnel flow conditions over a flat plate. The characteristic length in our computational domain is represented by the boundary-layer displacement thickness of the similarity solution at the inflow boundary, $\delta^* = 1$ mm, which is based on a distance from the plate leading edge of about 127 mm and an estimated boundary-layer thickness of $\delta^*_{99} \approx 1.25$ mm, from Van Driest's empirical correlations [49, 50] at the considered Mach number. Figure 1 represents the computational domain boundaries in a xy-plane (dashed line of the rectangular box) and a simplified sketch of the shock-transitional-boundary-layer interaction. The boundary-layer edge (denoted as BL in the sketch) is laminar near the inflow (left) boundary. The notations IS, SS and RS indicate the incident shock, separation shock and reattachment shock, respectively. The series of converging lines connecting with the separation shock indicate the weak compression waves generated by the concave curvature of the separation bubble edge, which coalesce into the separation shock. Similarly, the corresponding converging lines along the concave portion at the tail of the separation bubble indicate the compression waves coalescing into the reattachment shock. The series of dashed lines just downstream of the point of maximum thickness of the separation bubble, represent the expansion fan forming along the convex portion of the separation bubble edge. Immediately downstream of the reattachment shock, the boundary layer reattaches to the wall (bottom boundary, $y = 0$) and is depicted as a turbulent boundary layer, since the SBLI promotes rapid transition. Simulations are carried out at the freestream Mach number M = 5, temperature $T^*_\infty = 76.6$ K and Reynolds number Re = 12600, based on the boundary-layer displacement thickness at the inlet, and for isothermal wall with wall temperature $T^*_w = 290$ K. The total pressure and temperature in the freestream are, respectively, $p^*_0 = 864$ kPa and $T^*_0 = 460$ K. The freestream and wall temperature conditions are the same as in the studies of Cerminara et al. [47, 48]. Periodic conditions are imposed at the side boundaries (along the spanwise direction). The flow is initialised with the similarity boundary-layer solution for a Mach 5 flow at the specified wall temperature, whereas extrapolation, integral and zero-gradient outflow conditions are set at the inlet (left), top and outlet (right) boundaries, respectively. The streamwise position x_s in figure 1 indicates the location of the oblique incident shock generator imposed on the top boundary.

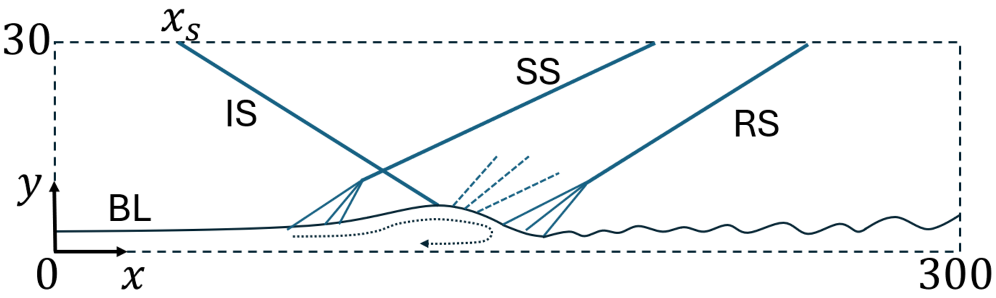

Fig. 1 Sketch of the shock/boundary-layer interaction within the computational domain, and illustration of the main shock wave system

Disturbance waves are imposed at the wall in the upstream laminar region to induce the transition process. These represent the most unstable modes for the present boundary layer identified in a former LST study shown in the work of Cerminara et al. [48]. In particular, in this work it was found that the most unstable modes are represented by both 2D and 3D waves pertaining to the class of the first instability modes, with streamwise wavenumber $\alpha = 0.2$, corresponding to a dimensionless streamwise wavelength of 31 and at the frequency $f = 12.5$ kHz. The most unstable 3D first mode was found at the spanwise wavenumber $\beta = 0.78$, corresponding to a dimensionless wavelength of 8 in the spanwise direction. The domain size in the spanwise direction has been set as a multiple of this wavelength, i.e. $L_z = 48$, allowing the development of lower spanwise wavenumber modes within our computational domain. The disturbance field imposed on the wall consists of the following wave function for the spanwise velocity component, which has been observed in previous studies [51] to induce a rapid transition to turbulence process:

$$w(x, z, t) = A_w \sum_{k=1}^{3} \left[\sin\left(\frac{2\pi k(z - z_0)}{l}\right)\right] \sin\left(\frac{2\pi(x - x_0)}{\lambda}\right) \sin(\omega t), \tag{8}$$

with $x_0 = 10$, $z_0 = 20$, $A_w = 0.2$, and $l = 8$ and $\lambda = 31$ representing the characteristic lengths of the disturbances in the spanwise and streamwise directions, respectively. In particular, a superposition of three oblique modes has been considered, with wavelengths l, $2l$ and $3l$ in the spanwise direction. The corresponding spanwise wavenumbers are within the wavenumber range of the 3D Mack's first modes found from the former LST study [48]. The wave function starts at $z = 20$ and terminates at $z = 28$ in the spanwise direction, whereas it spans the coordinate range $x = 10 - 41$ along the streamwise axis. A dimensionless frequency of 0.26, in the form of a Strouhal number, i.e. $f\delta^*/U^*_\infty$, has been used for the imposed disturbances, which corresponds to the above-mentioned dimensional frequency of the most unstable modes of the laminar boundary layer, i.e. $f = 12.5$ kHz [48].

At the top boundary a shock generator based on direct application of the Rankine-Hugoniot relations is imposed at the position x_s (see figure 1), corresponding to an oblique shock generated by a 8-deg half-wedge angle at Mach 5. Simulations are performed for both the cases of fixed shock and oscillating shock. In the fixed-shock case, the shock generator is at the distance $x_{s,f} = 31$ from the inlet boundary (where the subscript f stands for fixed). In the oscillating shock case, a time-periodic streamwise displacement of the shock generator is imposed at a given frequency. In particular, simulations have been conducted at three different frequencies, namely 11.5, 23 and 46 kHz, within a frequency range comparable to that predicted by Sawant et al. [37] for the shock bimodality at different Mach numbers. In their DSMC simulations, Sawant et al. [37] have obtained monotonically increasing frequencies from about 12 kHz to 37 kHz, for corresponding monotonically increasing Mach numbers from 3 to 10. Their DSMC-predicted frequency at Mach 5 is $f = 23$ kHz [37]. Hence, we consider the latter as the reference frequency for our study, whereas simulations at half (11.5 kHz) and double (46 kHz) the reference frequency will allow to identify the sensitivity of the solution within the main above-mentioned DSMC-predicted frequency range [37]. It should be mentioned that Sawant et al.'s [37] study considered normal shocks only. However, in the present study, which deals with oblique shocks in a STBLI case, we have assumed that the shock angle does not provide a significant change of the shock oscillation frequency outside of the considered frequency range (from 11.5 to 46 kHz). The present assumption is verified from the very recent DSMC study of Karpuzcu et al. [41] for the shock-layer unsteadiness downstream of oblique shocks over compression-expansion ramp geometries. In their study, Karpuzcu et al. [41] have obtained an oscillation frequency of 19.2 kHz for a Mach 6 flow at a ramp angle of a 42° and freestream velocity of 864 m/s. In our case, the freestream conditions correspond to a freestream velocity of 877.6 m/s, comparable to that in Karpuzcu et al.'s [41] work. On the other hand, the oscillation frequency predicted by Sawant et al. [37] at Mach 6 is 25 kHz, i.e. very similar to the value of 23 kHz at Mach 5, and relatively close to the value of 19.2 kHz predicted for the oblique shock case in [41]. Although the corresponding ramp angle (10°) of the incident shock, for the present case, is significantly different to the above ramp angle [41], Karpuzcu et al.'s [41] results have nonetheless proven that an oblique shock case at a generic ramp angle produces oscillation frequencies of the same order and in the same frequency range as those observed for normal shocks in [37]. Hence, whilst a systematic study of the effect of the shock angle, in a broad shock angle range and for different Mach numbers, should be subject of future investigation aimed at obtaining a complete dataset of configuration-specific oscillation frequencies, we will assume, for the purposes of the present work, a frequency of 23 kHz as a valid approximate representative frequency for our Mach 5 case.

The periodic (sinusoidal) function which simulates the streamwise displacement of the shock generator is given as

$$x_s(t) = x_{s,f} + A \sin \frac{2\pi t}{T_p}, \tag{9}$$

where $x_s(t)$ is the streamwise position of the shock generator on the top boundary at each given instant of time, $x_{s,f}$ is the position of the fixed shock (i.e. $x_{s,f} = 31$), A is the assigned amplitude, t is the dimensionless time and T_p is the dimensionless period of the shock oscillations (which matches that of the DSMC study [37]). Three different values of the amplitude A, namely $A = 1, 2, 3$, are arbitrarily selected to investigate the associated response of the SBLI dynamics to the impinging shock oscillation and its frequency. In addition, simulations have been carried out for two other frequencies, namely half ($f = 11.5$ kHz) and double ($f = 46$ kHz) the reference frequency of the DSMC study of Sawant et al. [37], with the aim to analyse the sensitivity of the solution to the shock-oscillation frequency.

B. Grid requirements for DNS resolution

The mesh size in the different directions is $N_x = 1874$, $N_y = 201$, $N_z = 360$, and a grid stretching in the vertical direction towards the wall has been applied in order to accurately resolve the boundary layer. The present grid provides values of $\Delta y+ = 0.38$, $\Delta x+ = 9.06$, $\Delta z+ = 7.54$ at $x = 290$ within the fully developed turbulent region, hence guaranteeing DNS resolution in all the directions, according to the work of Coleman and Sandberg [52], being the thresholds 1, 15 and 8 for $\Delta y+$, $\Delta x+$ and $\Delta z+$, respectively. To further assess the requirements for DNS accuracy, we considered an additional criterion, i.e. that described in the work of Yang et al. [53] for capturing rare high-intensity wall shear stress events. In particular, a grid resolution requirement dependent on the friction-based Reynolds number is presented for both $\Delta x+$ and $\Delta z+$ in the work of Yang et al. [53], and our considered values of $\Delta x+$ and $\Delta z+$ are within their indicated threshold values for resolving 99 % of the wall shear-stress events at a calculated friction Reynolds number of $Re_\tau = 283$, based on the δ_{99}, within the downstream turbulent region.

Furthermore, our calculated values of $\Delta y+$, $\Delta x+$, and $\Delta z+$ are in a reasonably good agreement with corresponding values from different published DNS studies of compressible flows in a Mach number range $M = 2 - 3$, reported in the work of Wenzel et al. [54]. In our case, the Mach number downstream of the wall-reflected shock, from inviscid oblique shock theory, is about 3.6, hence the Mach number range in [54] can be reasonably considered as relevant for our study. In particular, values in the range of $\Delta y+ = 2.3$ - 3.7, $\Delta x+ = 6.2$ - 9.9, and $\Delta z+ = 2$ - 3.2 are documented for the most conservative DNS of Wenzel et al. [54], within the friction Reynolds number range $Re_\tau = 140$ - 482. Whereas, other DNS studies reported for comparison are associated with generally larger values, e.g. $\Delta y+ = 0.48$, $\Delta x+ = 8$ - 24.6, and $\Delta z+ = 3$ - 12.6 [54]. In the DNS study of Duan et al. [55], in which supersonic Mach numbers from 3 to 12 were considered, values of $\Delta y+ = 0.25$ - 0.3, $\Delta x+ = 6.7$ - 8.4, and $\Delta z+ = 2.6$ - 3.4 are reported, however at larger friction Reynolds numbers, e.g. $Re_\tau = 376.8$ - 486.9. We can, hence, conclude that our calculated values $\Delta y+ = 0.38$, $\Delta x+ = 9.06$, $\Delta z+ = 7.54$ are sufficiently within the range reported in the literature for similar DNS studies at moderate supersonic Mach numbers and within the range of relevant friction Reynolds numbers. This, observing also that the flow is laminar and transitional for most of our computational domain streamwise extent, with turbulent flow reached in the downstream region, demonstrates that our grid fully satisfies the requirements for accurately resolving the flow features of the considered shock-transitional boundary-layer interaction phenomenon.

C. Validation study and application of shock oscillations to an experimental case

In the present section, we show results for a validation study based on existing experimental data of a transitional shock/boundary-layer interaction from the study of Currao et al [34]. The experiment consisted of a Mach 5.8 flow at a unit Reynolds number of 7×10^6 m^{-1} in the free-piston compression-heated Ludwieg tube at the University of Southern Queensland, over a flat plate with an impinging shock induced by a wedge-shaped shock generator with 10° flow deflection.

We model the experimental configuration through a flat-plate computational domain with mesh size and boundary condition as those described in Section III, with exception of the top boundary, where, in addition to the shock generator (described in Section III), we also apply a model for the concentrated expansion fan released at the trailing edge of the wedge as in the real experiment. In particular, the flow through the trailing-edge expansion fan is approximated via the Prandtl-Mayer flow solution for a 10° deviation angle.

Figure 2 shows the computational domain with instantaneous contours of the temperature and x-wise velocity in the midspan ($z^* = 24$ mm) xy-plane. The illustrations "S" and "E" within figure 2a indicate the locations of the incident shock and concentrated expansion fan on the top boundary. The lengths are presented in dimensional units consistent with the work of Currao et al [34]. It should be noted that the values along the horizontal axis represent the distance from the plate leading edge. The figure clearly shows the separation bubble, the incident-separation-reattachment shock wave system, the decrease of temperature and increase of velocity across the trailing-edge expansion fan, and a turbulent boundary layer generated downstream of the reattachment point (located at about $x^* \approx 130$ mm).

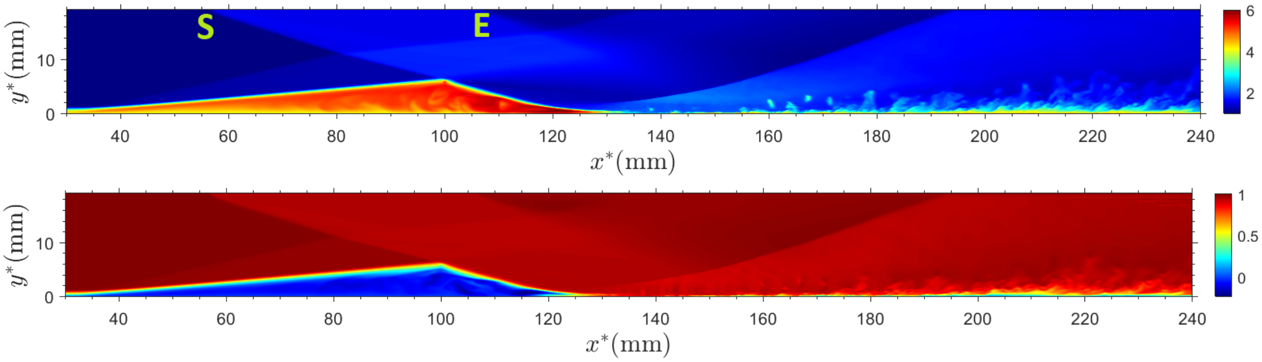

(a)

(b)

Fig. 2 Instantaneous temperature (a) and streamwise velocity (b) fields in the midspan ($z^* = 24$ **mm)** xy**-plane (no shock oscillations)**

Figure 3 shows contours of the instantaneous temperature and streamwise velocity fields inside the boundary layer. An evident flow pattern consisting of streamwise streaks forms near the reattachment location ($x^* \approx 130$ mm), which is a feature observed also in the experimental results [34]. Consistent with the experimental observations, the reattachment vortices are seen to propagate and break down downstream of about $x^* \approx 140$ mm into a fragmented structure indicating the transition process.

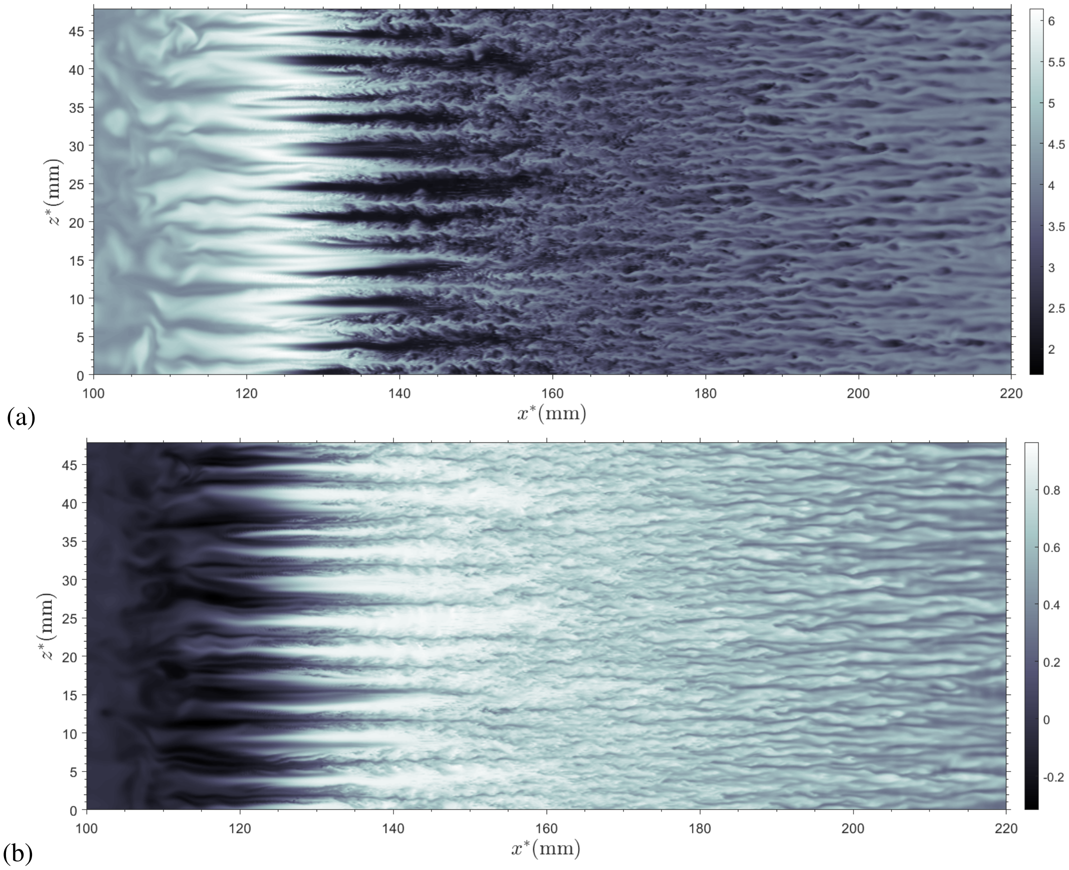

Fig. 3 Instantaneous temperature (a) and streamwise velocity (b) patterns within the boundary layer in the xz-plane at $y^* = 0.8$ mm (no shock oscillations)

Figure 4 shows the comparison between our DNS results and the experimental results of Currao et al [34] for the mean wall-to-freestream pressure ratio and Stanton number profiles along the surface. Numerical results in the hypothesis of laminar flow from Currao et al [34] are also included. It should be mentioned that in the reference work [34] the experimental data appear to be affected by a large uncertainty range, particularly in the plateau zone between the peak of both wall pressure and Stanton number profiles, and the start of their decay (due to the expansion fan impinging on the boundary layer), hence approximately within $130 < x^* < 160$ mm. In our work, the experimental data have been extracted from the upper region of the uncertainty range, following the curve described by the upper edge of the experimental profile. This, in turn, is reasonably close, as shown in figure 4a, to both our numerical results and the laminar results in the above-mentioned plateau region, as well as to the theoretical value of the pressure ratio from the oblique shock relations for the present flow case, $(p/p_\infty)_{th} \approx 10$. Our numerical results agree with both the theoretical predictions as well as the laminar curve for the peak of the pressure ratio, and follow very well the experimental profile both along the increasing branch and the decay branch. Results for the Stanton number in figure 4b show a large difference between our numerical results and the numerical laminar results from the reference work [34], with the exception of the initial region upstream of the shock impingement location, where both curves match. This is reasonable if we consider that flow undergoes transition to turbulence induced by the shock/boundary-layer interaction, which has a dramatic effect on the heat flux. In the assumption of laminar flow, a larger separation bubble and a lower peak of the surface heat flux are to be expected, which is what is shown indeed by the red curve in 4b. Our results, in contrast, show that the Stanton number starts from its laminar value, as the boundary layer is still laminar in the upstream region, then, as the flow undergoes transition across the reattachment, the profile detaches from the laminar prediction and agrees better with the experimental data reaching higher values. Our numerical curve shows a larger peak of the Stanton number compared to the experiments (similarly to what observed for the pressure ratio), but agrees very well with the experimental curve in the following decreasing region.

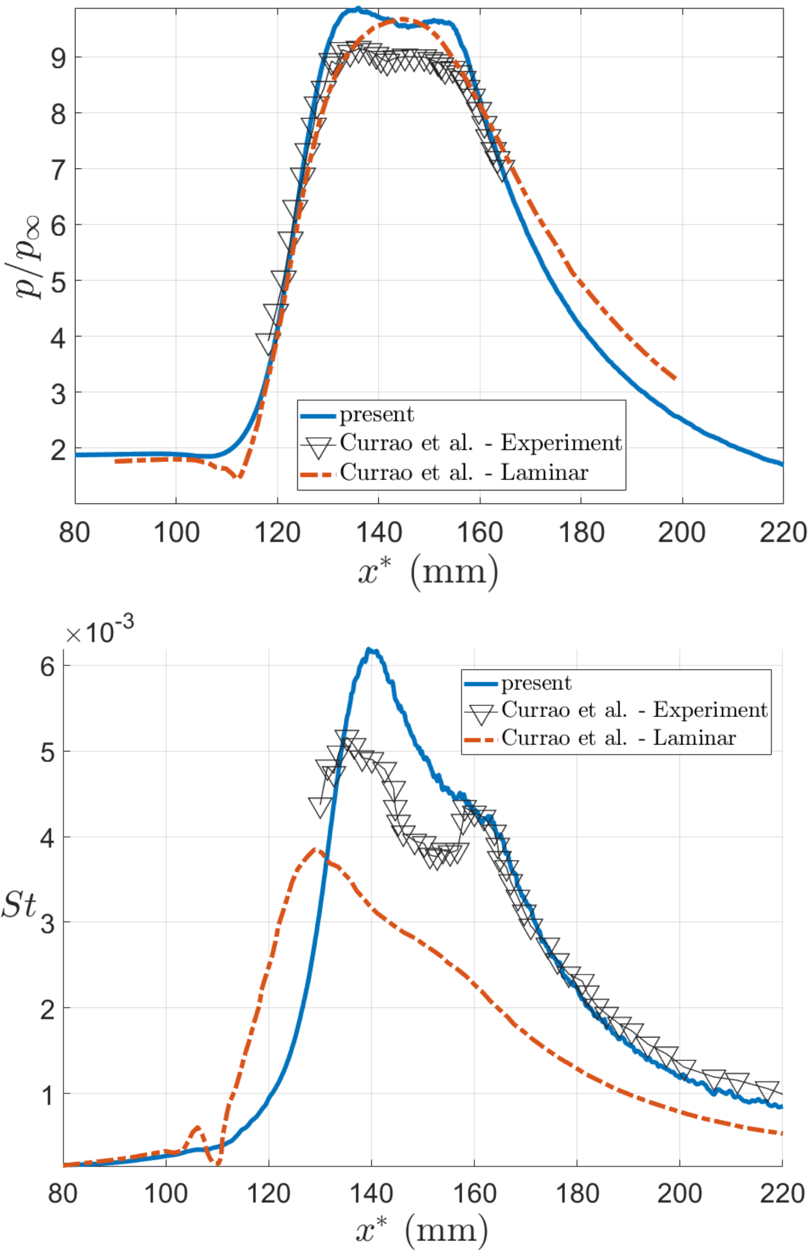

(a)

(b)

Fig. 4 Mean wall pressure (a) and Stanton number (b) profiles on the surface

Figure 5 shows a comparison of flow patterns for the surface heat-flux fluctuations between our DNS and the experimental results. Figure 5a has been extracted from Currao et al's work[34] and represents the fluctuation field of the surface heat flux from the experimental observations. It should also be mentioned that the orange band seen in 5a indicates the distance between the two consecutive peaks of the double-peak Stanton number profile as shown by the experimental data (see figure 4). In this case, the distance from the leading edge is indicated along the vertical axis, while the horizontal axis indicates the spanwise direction. The corresponding numerical results from our DNS are plotted in Figure 5b. It is important to notice that the spanwise extent of our computational domain does not span the whole width of the probe in the real experiment. As can be seen, our DNS capture a very similar flow pattern observed in the experiments, which consists of elongated streamwise streaks of heat-flux fluctuations developing downstream of the reattachment location ($x^* \approx 130$ mm). These are correlated with the reattachment vortices seen in figure 3, and are seen to gradually break down into secondary streaks further downstream throughout the transition process. Both amplitude and average spanwise wavelength ($\lambda^* \approx 5$ mm) of the heat-flux oscillation streaks are in a good agreement between our numerical results and the experiments.

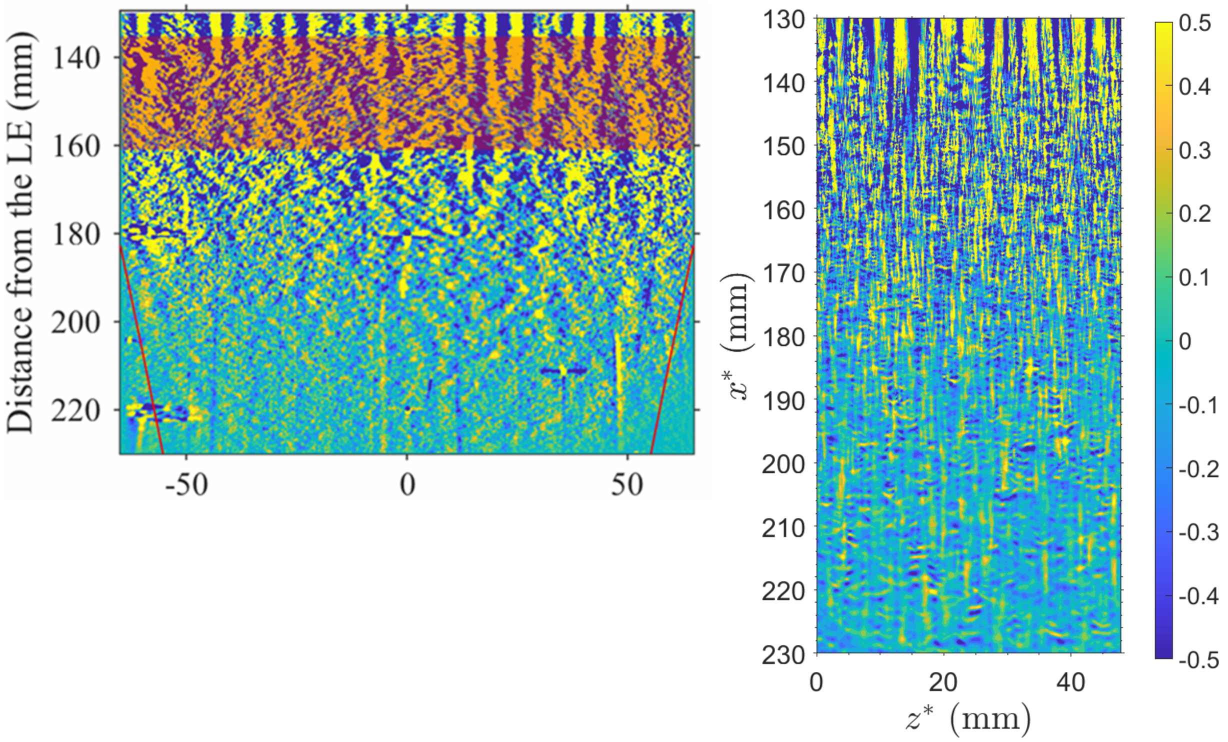

Fig. 5 Surface heat-flux fluctuation (kW/m^2) patterns: reference experiment (a), present numerical results (b)

IV. Results

The present section is divided into four subsections. In IV.A results for the main Mach 5 flow field with no shock oscillations (or a fixed shock only) are presented; IV.B show the response within the shock layer for the case with shock oscillations at different frequencies; finally IV.C presents results for the response at the surface at different frequencies and amplitudes.

A. Main flow characteristics with fixed impinging shock

We will be showing here results depicting the main flow features of the considered SBLI case with no oscillations imposed on the shock.

Figure 6 shows a numerical Schlieren image in the midspan xy-plane and inside the boundary layer (on a xz-plane), at the height $y = 1$ off the wall. The numerical Schlieren image has been obtained by plotting the magnitude of the density gradient at each point within the xy-plane at the midspan of the computational domain, as $\sqrt{(\partial\rho/\partial x)^2 + (\partial\rho/\partial y)^2}$. The Schlieren plot in figure 6(a) shows details of the shock structure within the SBLI, as well as the boundary-layer edge in the laminar upstream region, the edge of the separation bubble prior to the incident shock and the turbulent boundary layer downstream of the reattachment shock, with reattachment point located at $x \approx 126$. Illustrations are added to the figure to clearly indicate the incident shock (IS), the reattachment shock (RS), as well as the shock layer downstream of the incident shock (SL1) and the shock layer downstream of the reattachment shock (SL2). This will be particularly useful for the description of the flow details in the next section. The light gray line propagating upwards downstream of the incident shock represents the separation shock (SS) formed upstream due to the separation bubble. The separation shock is much weaker than the incident shock and the reattachment shock, hence when we will refer to the shock layer downstream of the incident shock (SL1) we will not distinguish between the flow upstream and downstream of the separation shock, i.e. we will consider SL1 the whole flow field enclosed between IS and RS. On the other hand, the Schlieren image in figure 6(b) depicts details of the boundary-layer transition, rapidly enhanced by the shock/boundary-layer interaction, and the turbulent flow features immediately downstream of the reattachment point up to the end of the computational domain.

Figure 7 represents the time-averaged and spanwise-averaged profiles of the streamwise skin-friction coefficient and the Stanton number. As can be seen, near the inlet the skin-friction coefficient matches with that of the laminar similarity boundary-layer solution, then it decays assuming negative values indicating the start of the separation bubble, and increases rapidly at the reattachment point ($x \approx 126$) approaching the turbulent correlation [49, 50], which is indicative of a rapid transition process in this region. This follows a gradual decrease further downstream with the growth of the turbulent boundary-layer thickness. The computed separation bubble length is about $l_b \approx 96$. The Stanton number shows a similar trend, but with a more pronounced decrease in the downstream region after having reached the peak just downstream of the reattachment point. The profiles for the skin friction and Stanton number shown in figure 7 are consistent with the expected trends for a case of transitional shock/boundary-layer interaction (similar trends can be seen, e.g., in the work of Sandham et al. [10] for a Mach 6 flow).

Figure 8 shows the corresponding time-averaged and spanwise-averaged wall pressure profile. As can be seen, the pressure increases through the separation bubble reaching the first plateau at about $x \approx 75$, and then increases again by a much larger extent across the shock impingement/reattachment region. The wall-pressure to freestream-pressure ratio reaches a value of 5.42 at the position $x = 200$ downstream of the reattachment, which is sufficiently close to the theoretical value of 5.44 from the oblique shock relations.

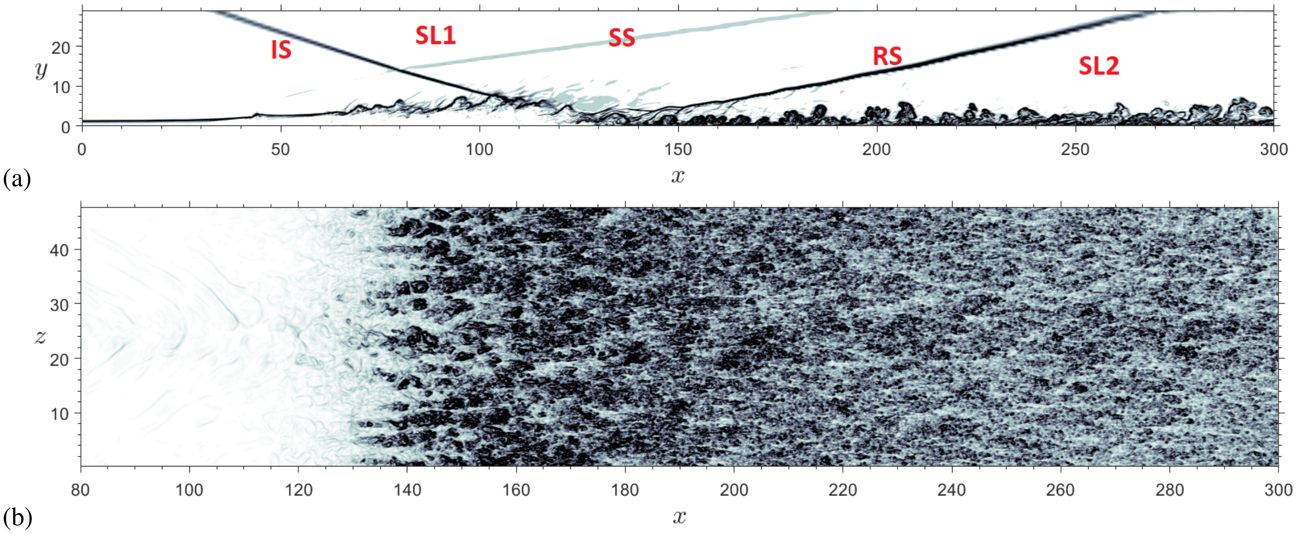

Fig. 6 Instantaneous Schlieren view in a xy-plane (a) and in a xz-plane within the boundary layer (b)

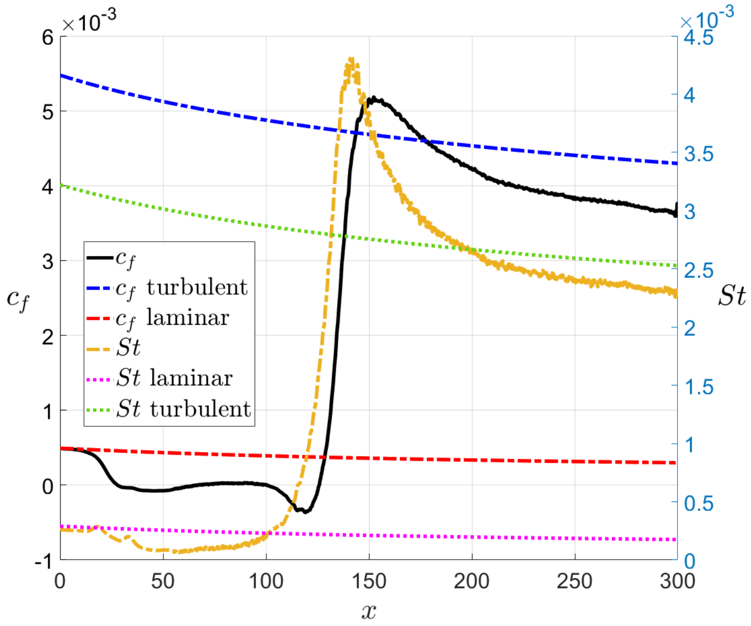

Fig. 7 Profiles of time-averaged streamwise skin-friction coefficient and Stanton number on the surface

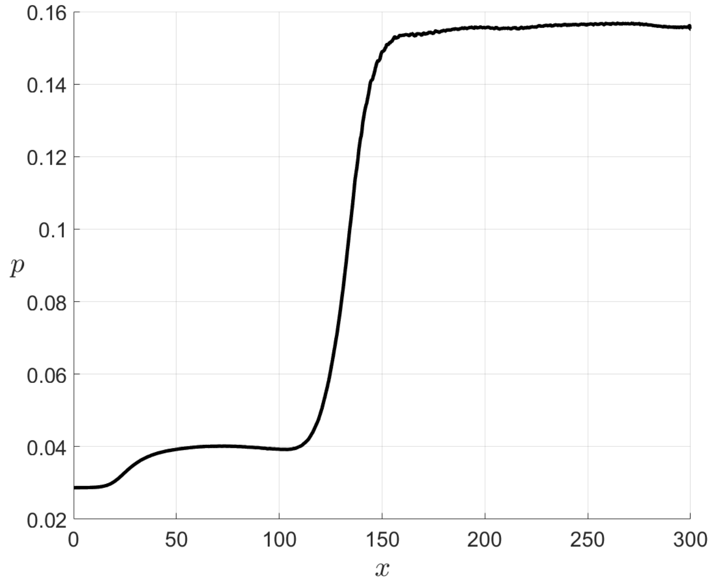

Fig. 8 Time-averaged wall (y = 0) pressure

Figure 9 represents the field of pressure fluctuations in the midspan xy-plane for the non-oscillatory case at the reference Fast-Fourier transformed frequencies considered for the shock oscillations (i.e. 11.5 kHz, 23 kHz and 46 kHz). As can be seen, an unsteadiness of the SBLI phenomenon is present without shock oscillations, which is mostly confined within the separation bubble, the impingement location and the region immediately downstream of the reattachment shock. All the three different frequencies show similar patterns, in general, although with some differences in terms of intensity of specific features. There is evidence, especially at the lower frequencies (11.5 kHz and 23 kHz), of waves radiated in the SL1 region downstream of the separation shock, which are correlated to the unsteadiness of the separation bubble and the interaction region, as well as oscillations along the reattachment shock. The latter feature is more evident at the lowest frequency (11.5 kHz), in which pronounced oscillations of the reattachment shock can be observed, which also induce some wave fronts in region SL2 (i.e. downstream of the reattachment shock) . The response at 23 kHz, in contrast, shows more pronounced unsteadiness within the separation bubble and downstream of the separation shock, and an overall lower effect on the reattachment shock. At the highest frequency (46 kHz) pronounced unsteadiness appears concentrated in the interaction region, whereas lower amplitude effects can be barely seen in the other flow regions.

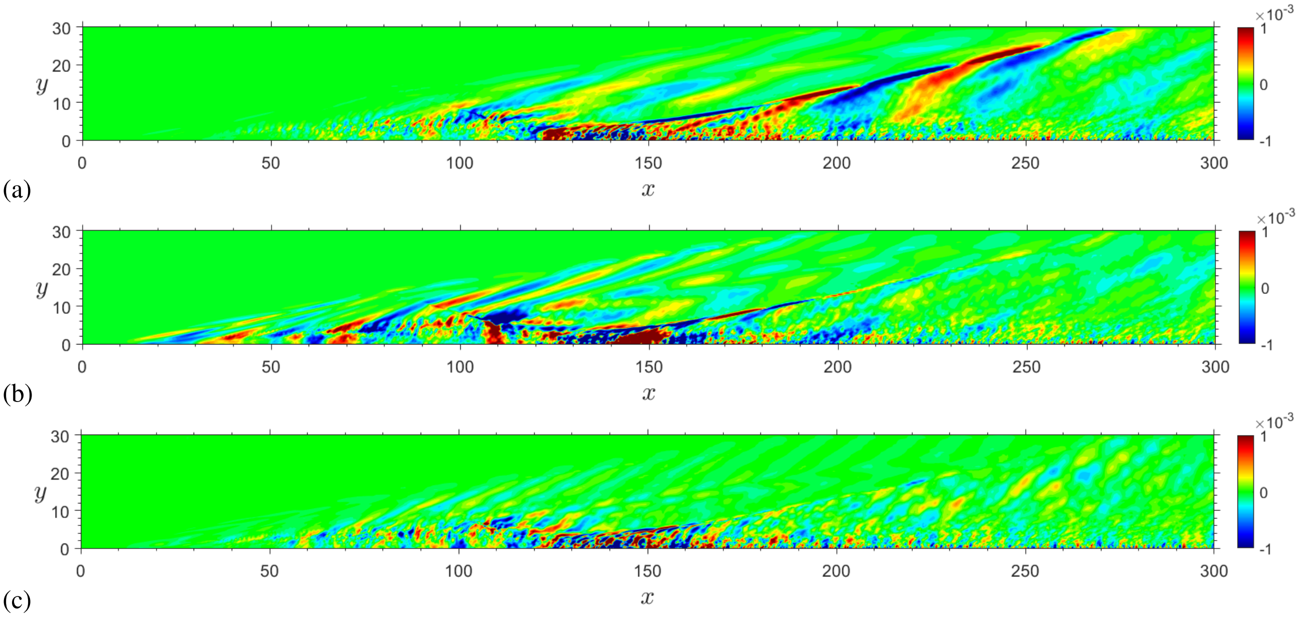

Fig. 9 FFT pressure fluctuations (real part) in xy-plane without shock oscillations. Response at 11.5 kHz (a), 23 kHz (b), 46 kHz (c)

B. Wave structure in the shock layer

We now analyse the patterns of the waves induced by the oscillatory shock in the shock layer downstream of the incident shock and the reattachment shock. Results shown in this section refer to simulations performed at different frequencies of the incident shock oscillations and at the highest amplitude, i.e. $A = 3$.

Figure 10 shows results for the pressure fluctuations for the case of incident shock oscillating at the lowest frequency (11.5 kHz), i.e. half of the reference DSMC-predicted frequency [37] of the natural shock oscillations for this Mach number. Different frequencies have been extracted through a Fast Fourier Transform (FFT) applied to the flow field, and, as can be seen, at the fundamental frequency of 11.5 kHz (figure 10a) the waves in the shock layer appear much more amplified compared to the larger frequencies, as expected. Oscillations are evident along the incident shock as well as along the reattachment shock, and a complex wave system, induced by the incident shock oscillations, appears transmitted in the shock-layer region between the incident and the reattachment shock. In particular, downstream of the separation shock, the wave fronts appear distorted (with amplified oscillations along the separation shock line) and aligned almost horizontally. The latter is an effect of waves generated within the separation bubble (see region $x < 100$), upstream of the impingement point, which are then transmitted across the incident shock and interact with the vertical wave fronts generated downstream of the incident shock. Then, downstream of the reattachment shock (i.e. in the second shock layer), a clearer wave structure of vertically-oriented wave fronts can be observed, which propagate downstream with a similar amplitude to that of the waves induced by the incident shock oscillations. This demonstrates that the waves generated just downstream of the oscillating incident shock are effectively transmitted downstream of the reattachment shock and propagate in the downstream region applying a forcing to the local boundary layer.

Figures 10b and 10c show that at higher frequencies, 23 kHz and 46 kHz, respectively, the disturbances in both shock layers SL1 and SL2 seem much weaker, and almost no oscillations can be observed along and just downstream of the incident shock. This suggests that the incident shock is able to radiate waves only at the fundamental frequency of the shock oscillations, whilst the low-amplitude waves present in SL1 and SL2 are mostly associated with disturbances originating within the separation bubble, in the shock impingement region, and along the reattachment shock. Indeed, in contrast to the incident shock, the reattachment shock shows evident oscillations also at different frequencies, although at a lower intensity compared to the fundamental frequency. This is due to unsteadiness of the separation bubble and the shock impingement and reattachment region, which is present also in the absence of shock oscillations (depicted in 9a, at the FFT frequency of 11.5 kHz). This unsteadiness is responsible for the low-amplitude waves transmitted in the SL1 region downstream of the separation shock, as well as for the oscillations of the reattachment shock, which, in turn, generate low-amplitude waves in SL2.

Overall, from the analysis of the disturbance features in figure 10, it can be concluded that the shock-layer wave structure at frequencies higher than the fundamental shock-oscillation frequency appears very similar to that for the case without shock oscillations, and is mostly due to the inherent unsteadiness of the shock/boundary-layer-interaction phenomenon. The wave structure at the shock-oscillation frequency is, in contrast, significantly more intense in amplitude, and with an evident effect of vertically-oriented wave fronts released by the oscillating incident shock and efficiently transmitted downstream of the reattachment shock and the downstream region.

Figure 11 shows the corresponding results for the case of oscillating shock at the frequency 23 kHz, i.e. equal to the DSMC-predicted frequency in the work of Sawant et al. [37]. Similar results can be observed, in general, as those discussed in figure 10. The wave patterns at the fundamental frequency (see figure 11b) reveal again an evident system of vertically-oriented amplified wave fronts generated by the oscillations of the incident shock, which first interacts with the waves downstream of the separation shock, and then gets transmitted across the reattachment shock into the downstream region (SL2). Similarly to figure 10, the response at the lower non-fundamental frequency (see figure 11a) resembles that for the case with no shock oscillations (in figure 9b). We notice, in this case, a high-frequency excitation in figure 11c, with evidence of shorter-wavelength oscillations of the incident shock and radiated post-shock wave fronts, which produce a similar mechanism as that observed in 11b at the fundamental frequency, however at a significantly lower amplitude. This may suggest that the imposed amplitude of the impinging shock oscillations is high enough to trigger nonlinear effects at the higher frequencies.

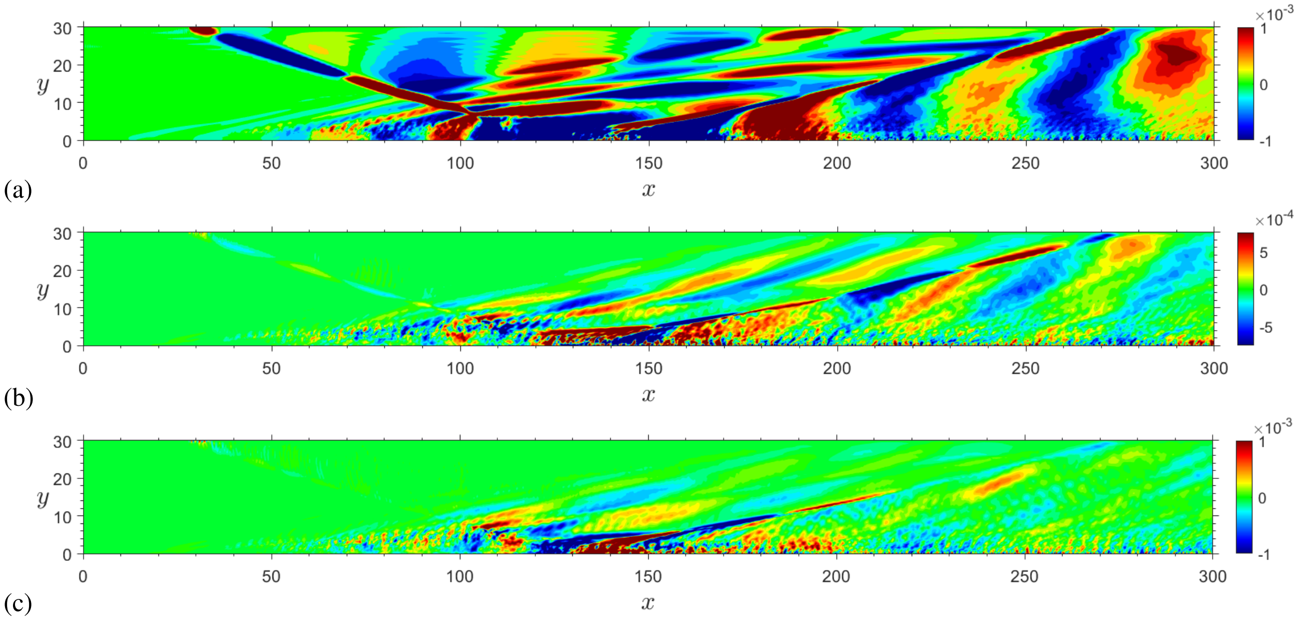

Fig. 10 FFT pressure fluctuations (real part) in xy-plane (fundamental frequency $f = 11.5$ kHz). Response at 11.5 kHz (a), 23 kHz (b), 46 kHz (c)

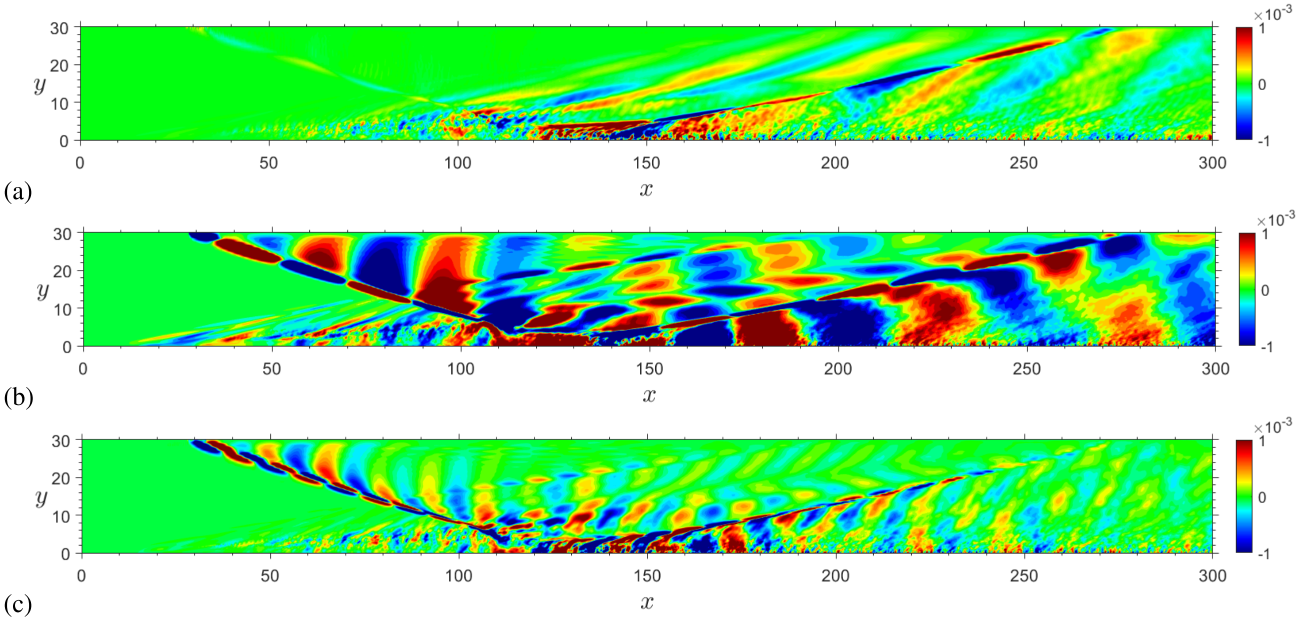

Fig. 11 FFT pressure fluctuations (real part) in xy-plane (fundamental frequency $f = 23$ kHz). Response at 11.5 kHz (a), 23 kHz (b), 46 kHz (c)

Figure 12 shows the results for the shock oscillation frequency of 46 kHz. Again, it is possible to notice similar patterns as those already discussed for the previous figures. The response at the fundamental frequency (figure 12c) shows wave fronts of consistently smaller wavelength compared to the previous cases at the lower fundamental frequencies. It should also be noticed that vertically-oriented wave fronts, generated by the incident shock oscillations, appear to dominate also the region downstream of the separation shock, in which there is no evidence of horizontally-oriented waves. This suggests that the latter flow feature is associated with the low frequencies of the shock oscillations. In region SL2, amplified waves propagate downstream of the reattachment shock forcing the local turbulent boundary layer. The response at the frequency 11.5 kHz (see figure 12a) shows similar flow patterns as those observed in the previous case at the same frequency (see figure 11a), with flow features resembling the case with no shock oscillations (see figure 9). The latter, in turn, shows a weaker wave structure at 46 kHz (figure 9c), compared to the lower frequencies, mostly located in the shock interaction region. The response at 23 kHz (see figure 12b) shows also a similar structure to that at 11.5 kHz, with no evidence of nonlinear effects along the incident shock. However, some wave amplification is observed in both regions SL1 and SL2, more precisely wave fronts downstream of the separation shock and immediately downstream of the reattachment shock. These, in turn, are correlated to the pronounced unsteadiness within the separation bubble and the impingement location, as shown in figure 12b. Similar features can be observed in general for the cases with no shock oscillations (e.g. see figures 9a and 9b), however at lower amplitudes.

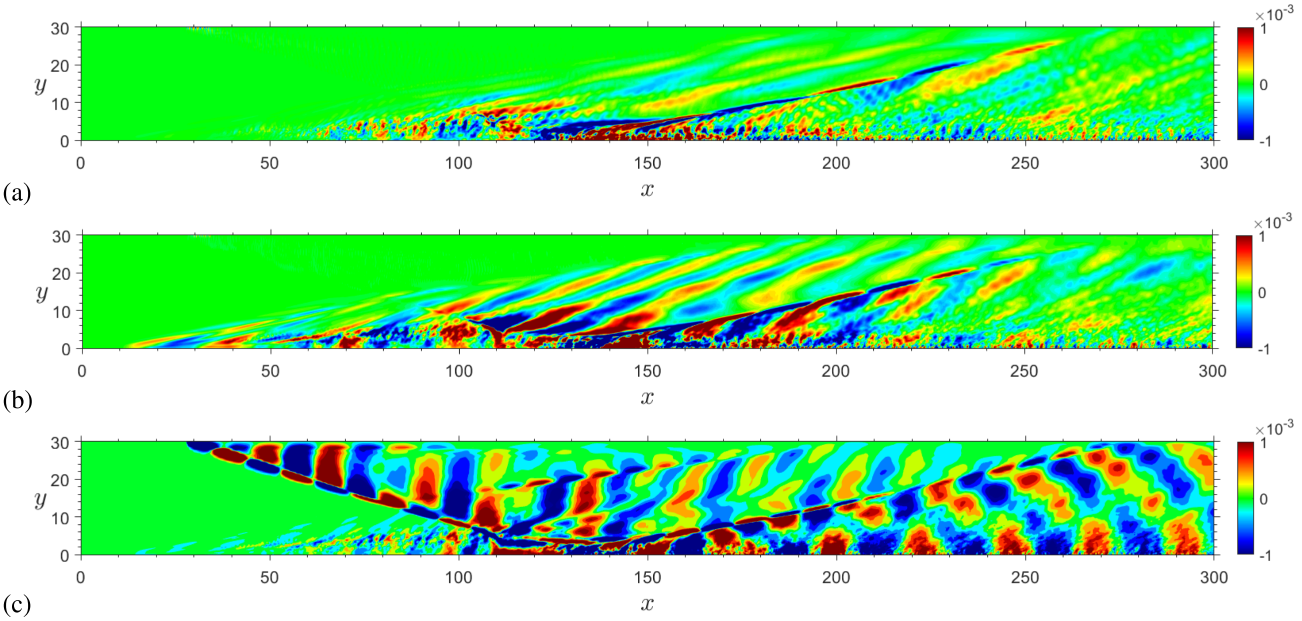

Fig. 12 FFT pressure fluctuations (real part) in xy-plane (fundamental frequency $f = 46$ kHz). Response at 11.5 kHz (a), 23 kHz (b), 46 kHz (c)

In order to evaluate the effect of the shock-oscillation amplitude on the solution, figures 13, 14 and 15 show the Fast-Fourier-Transformed response at the frequencies 11.5 kHz, 23 kHz and 46 kHz, respectively, with the reference $f = 23$ kHz as fundamental frequency, for different amplitudes of the shock oscillations ($A = 1, 2, 3$). Results show that, at each frequency the same overall wave structure is maintained for different amplitudes, with increasing values of the pressure fluctuations for increasing shock-oscillation amplitudes (note that the color scale has been kept constant across the different subplots in each figure). The wave structure in figure 13 appears very consistent with that shown in figure 9a at the same frequency (11.5 kHz) without shock oscillations, which is indication of absent or negligible nonlinear effects induced, at the lower frequencies, by the shock oscillations (at the fundamental frequency of 23 kHz). Figure 14 shows the response at the fundamental frequency of the shock oscillations (23 kHz), with the above-described coherent wave patterns induced in the downstream turbulent boundary layer, which are more pronounced at increasing amplitudes of the shock oscillations. Finally, figure 15a shows evidence of a nonlinear higher-frequency (46 kHz) excitation associated with the incident shock oscillations, which has a similar structure to the response at the fundamental frequency (23 kHz) in figure 14, however with shorter wavelengths (consistent with the higher frequency) and at a lower overall amplitude. Sign of small oscillations can be observed along the incident shock in figure 15a, which grow rapidly with the oscillation amplitudes forming a clear pattern of post-shock wave fronts downstream of the incident shock at the highest amplitude (15c).

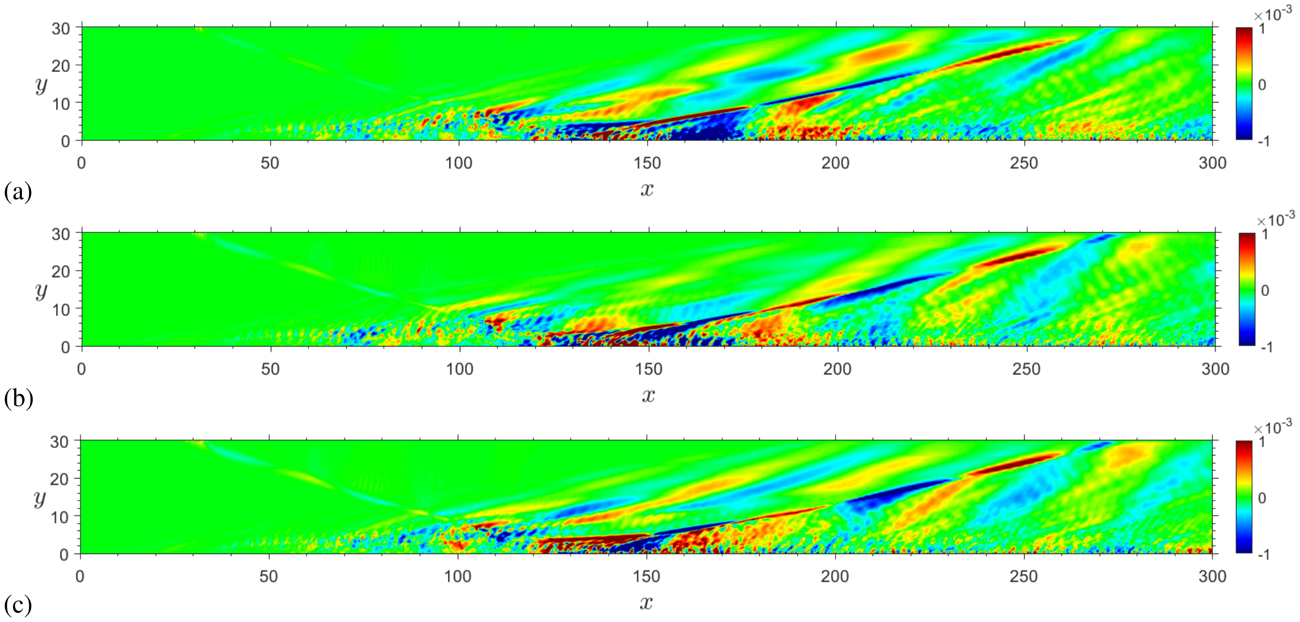

Fig. 13 FFT pressure fluctuation response (real part) in xy-plane at 11.5 kHz: $A = 1$ (a), $A = 2$ (b), and $A = 3$ (c)

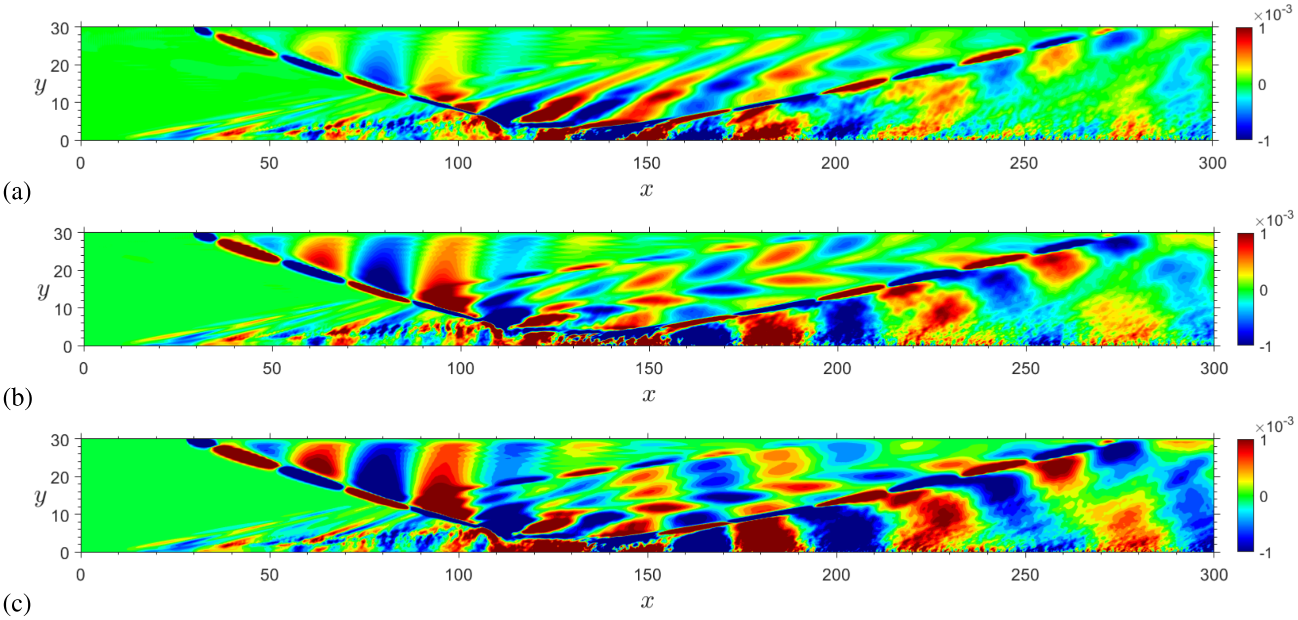

Fig. 14 FFT pressure fluctuation response (real part) in xy-plane at 23 kHz: $A = 1$ (a), $A = 2$ (b), and $A = 3$ (c)

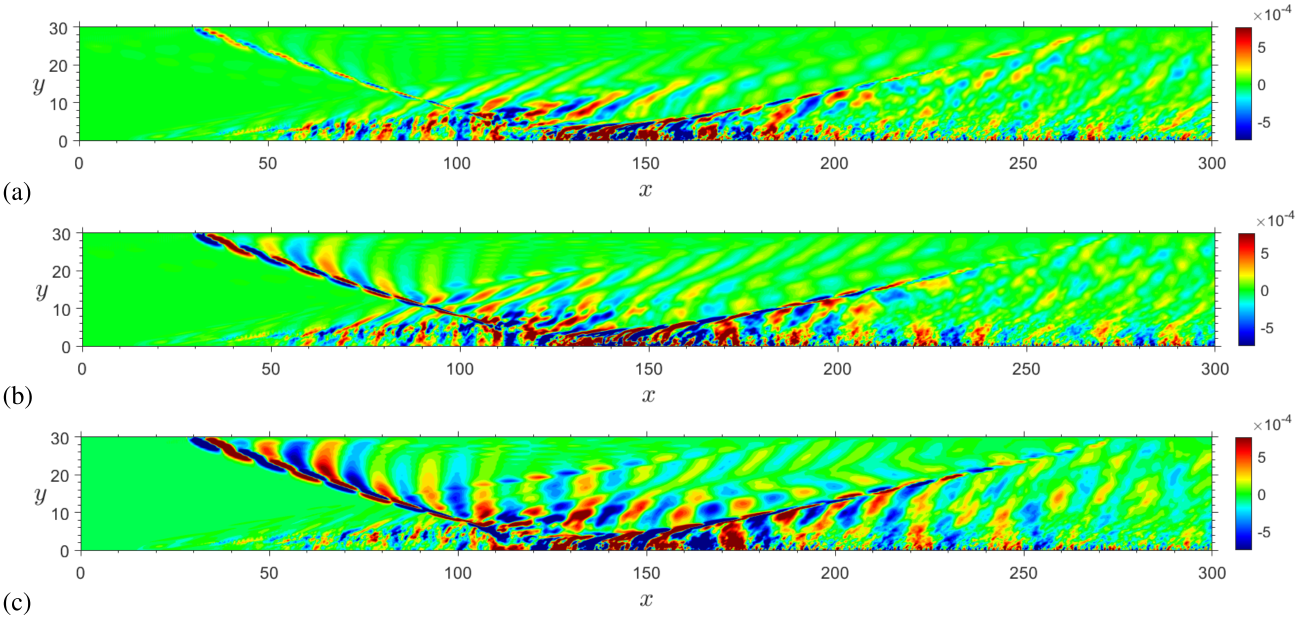

Fig. 15 FFT pressure fluctuation response (real part) in xy-plane at 46 kHz: $A = 1$ (a), $A = 2$ (b), and $A = 3$ (c)

C. Wall Response

We now move to the analysis of the pressure response on the surface. We will consider here, not only contour plots revealing the main flow patterns on the surface, but also spanwise-averaged profiles of the pressure-fluctuation distribution along the surface, which enable a more quantitative evaluation of the amplitude comparison at different frequencies as well as for different disturbance modes (e.g. 2D and oblique wave modes).

Figure 16a shows contours of the Fast Fourier transformed wall pressure fluctuations at the frequency of 23 kHz (i.e. the reference DSMC-predicted frequency at the present Mach number) for the case of no shock oscillations. This serves as a reference for comparison of the surface flow patterns with the other cases with oscillating shock. The pressure patterns shows turbulent boundary layer downstream of the reattachment point. Figure 16b shows the corresponding spanwise-averaged streamwise distribution of the pressure-fluctuation amplitude taken at different FFT frequencies. As can be seen, for the case of no shock oscillations, the wall-pressure response follows approximately the same trend at all the frequencies. A high peak is reached immediately downstream of the reattachment point, then the pressure fluctuations decrease towards a plateau in the downstream region.

Figure 17 shows the corresponding wall pressure fluctuation contours for the three oscillating-shock cases at the respective fundamental frequencies, namely 11.5 kHz, 23 kHz, and 46 kHz. It can be clearly observed that oscillations of the incident shock produce, at the fundamental frequency, a compact amplified 2D-wave structure which propagates downstream of the reattachment shock within the local turbulent boundary layer. The 2D waves show a decreasing wavelength from figure 17a to figure 17c, consistent with the increasing frequency of the shock oscillations. This wave pattern is completely absent in the case without shock oscillations depicted in figure 16a, and, as such, represents an effect of the incident shock oscillations on the downstream turbulent boundary layer, as well as the evidence of the efficient wave transmission mechanism from region SL1 to SL2, as discussed in the previous section. The shown wall response downstream of the reattachment point is indeed correlated to the local wave forcing within the shock layer SL2, which modulates the turbulent boundary layer.

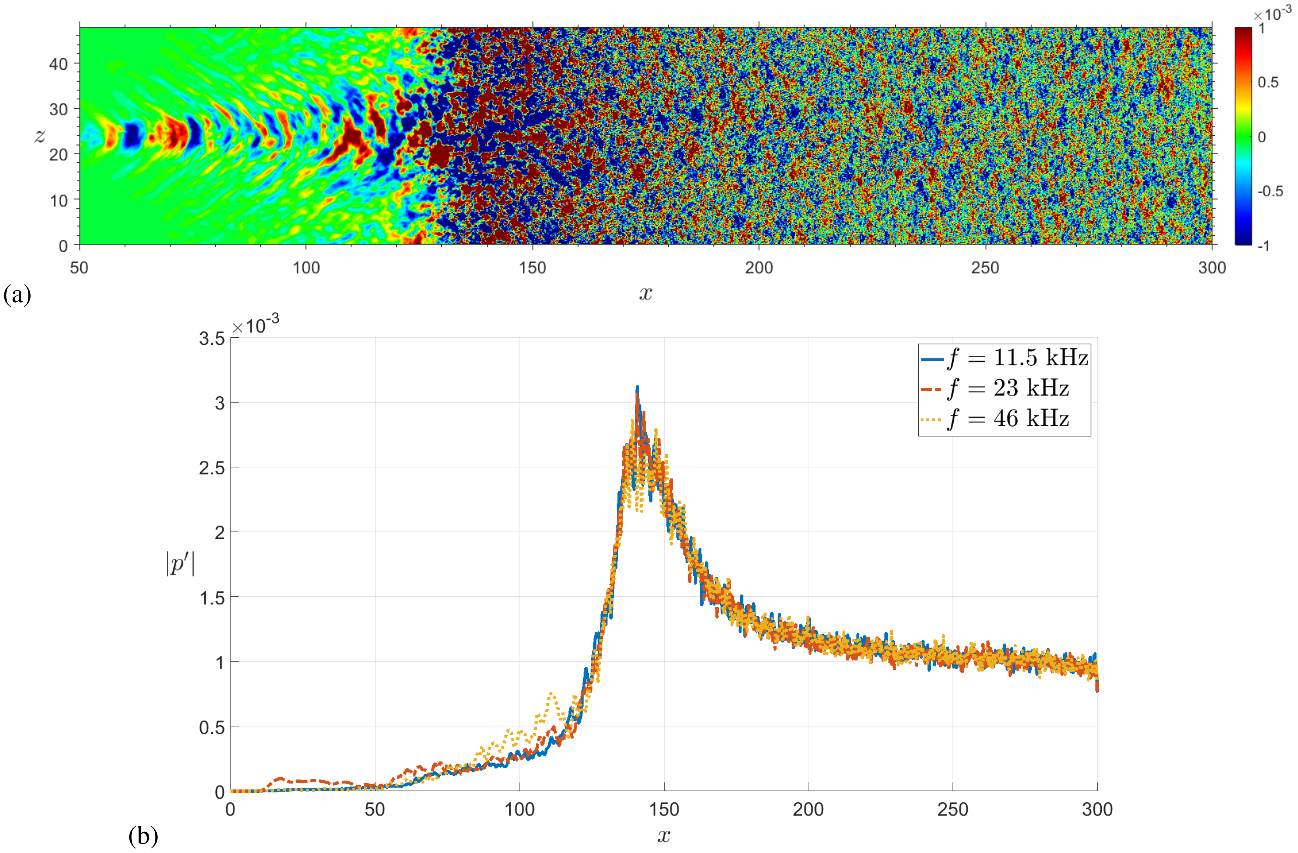

Fig. 16 FFT wall-pressure fluctuations without shock oscillations: real part distribution patterns at 23 kHz (a), and spanwise-averaged absolute value at different frequencies (b)

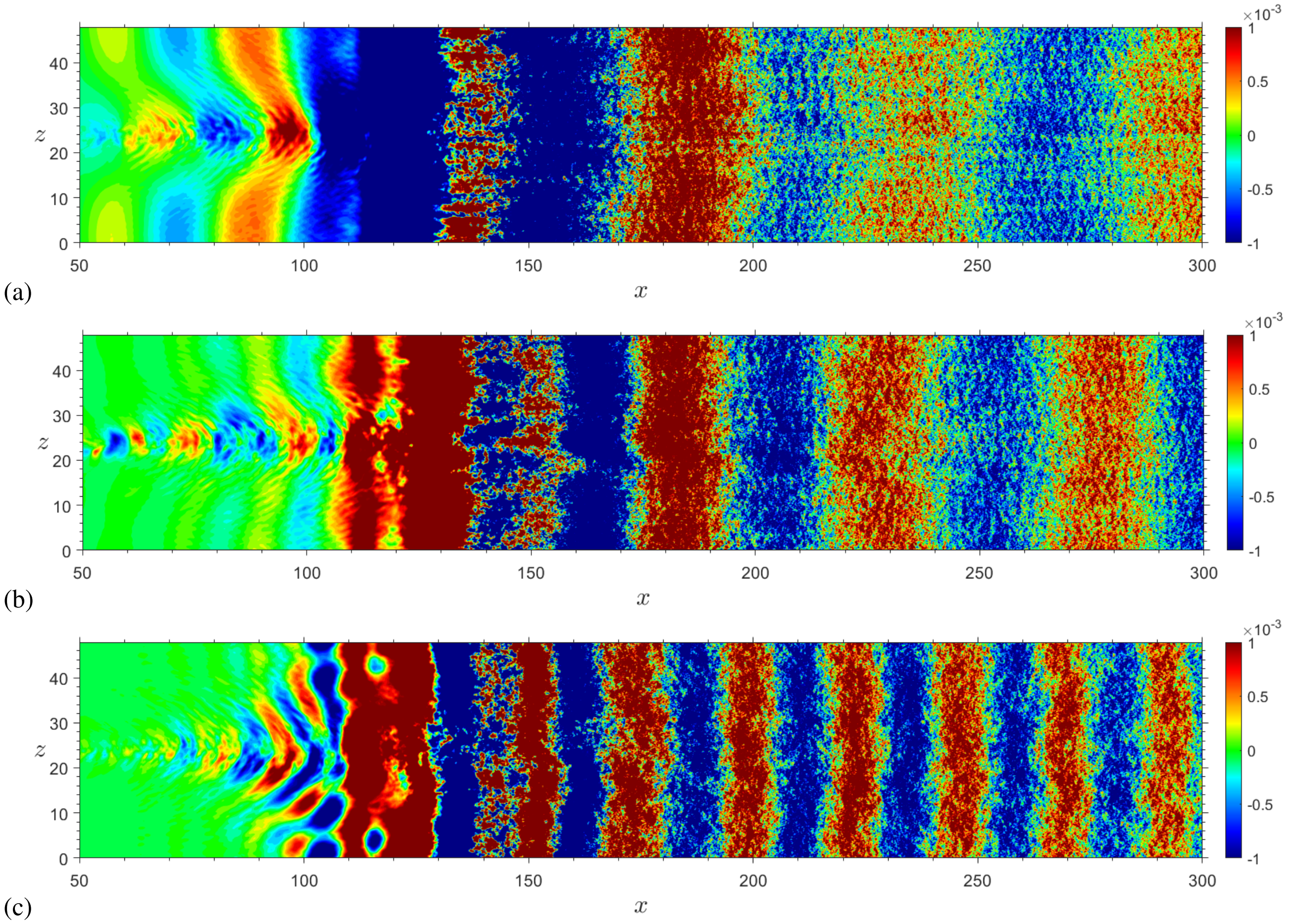

Fig. 17 FFT wall-pressure fluctuations (real part) at different fundamental frequencies ($A = 3$): 11.5 kHz (a), 23 kHz (b), 46 kHz (c)

Figure 18 shows the effect of the shock-oscillation amplitude on the wall-pressure fluctuation patterns at the fundamental frequency of 23 kHz. Each of the three different amplitudes ($A = 1, 2, 3$) shows evidence of the compact 2D wave structure modulating the turbulent boundary layer, thus demonstrating that the same wave transmission mechanism from region SL1 to region SL2 and in the downstream boundary layer originates for each of the considered amplitudes. As expected, the wave fronts propagating in the turbulent boundary layer appears more pronounced as the amplitude is increased.

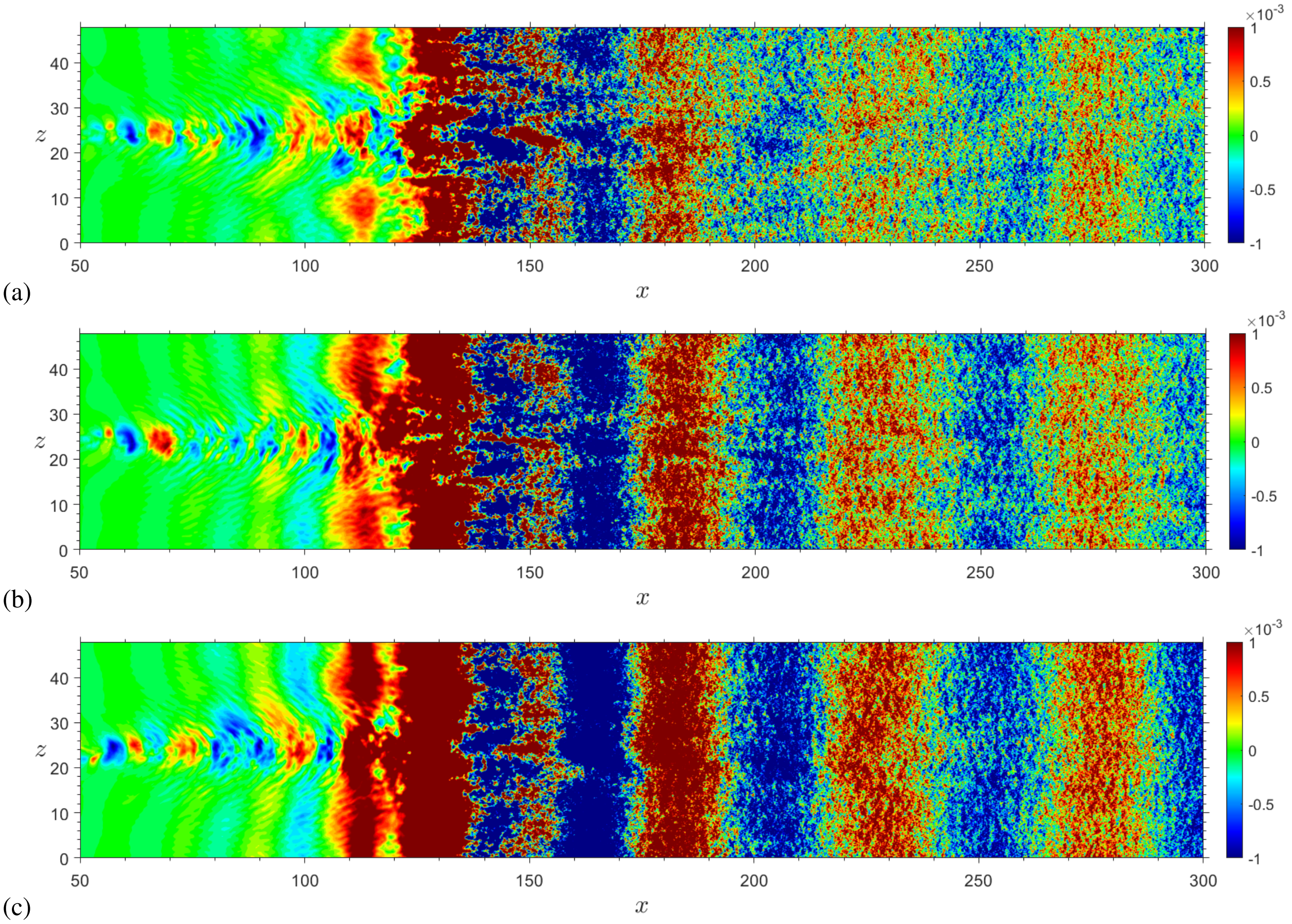

Fig. 18 FFT wall-pressure fluctuations (real part) at different amplitudes (fundamental frequency 23 kHz): $A = 1$ **(a),** $A = 2$ **(b),** $A = 3$ **(c)**

Figure 19 shows x-wise profiles of the frequency-dependent spanwise-averaged wall-pressure fluctuation amplitude for the three oscillating-shock cases at different fundamental frequencies. As can be seen, the effect of the frequencies different from the fundamental frequency (either subharmonics or superharmonics) is marginal for all the cases, and the related pressure-fluctuation profile is very similar to that for the case without shock oscillations (see figure 16b). However, at the fundamental frequency of the shock oscillations, the fluctuation amplitude shows a significant increase, both upstream (i.e. in the separation bubble) and downstream of the reattachment point, with a double-peak pattern. The location of the peaks is frequency dependent, with the lowest frequency (figure 19a) showing the first peak approximately at the reattachment point and the second higher-amplitude peak immediately downstream. At the larger frequencies (figures 19b and 19c), however, both main peaks of the double-peak structure occur downstream of the reattachment location, and the first one is also the highest one in amplitude. The maximum amplitude is also frequency dependent, with the higher frequencies (23 kHz and 46 kHz) showing a very similar amplitude peak, larger by about 20% than that for the lowest frequency (11.5 kHz). Furthermore, we notice that the response to the higher frequencies presents a third lower-amplitude peak located upstream of the reattachment point, which is more amplified at the highest frequency (46 kHz). Downstream of the reattachment point, the response at the fundamental frequency shows a significantly larger amplitude compared to different frequencies, as well as compared to the case without shock oscillations, for a relatively extended region (up to $x \approx 200$), before decreasing towards a plateau towards the end of the computational domain. However, at the highest frequency, the amplitude is seen to maintain a pronouncedly larger value compared to the other (non-fundamental) frequencies and the no-oscillation case throughout the whole domain extension in the downstream region. At the position $x = 230$, hence at a distance of approximately $\Delta x = 104$ from the reattachment point, the amplitude of the highest fundamental frequency is still about 50% larger than that at the different (non-fundamental) frequencies and the no-oscillation case, whereas at the end of the computational domain ($x = 300$) it is about 30% larger. We can conclude that shock oscillations promotes the emergence of a 2D-wave system propagating downstream with a sustained amplitude, whose amplification is larger at higher frequencies and span larger streamwise lengths. This, in turn, indicates that at frequencies equal to and larger than the DSMC-predicted frequency, the the wave transmission and amplification mechanism in region SL2 is stronger than at lower frequencies.

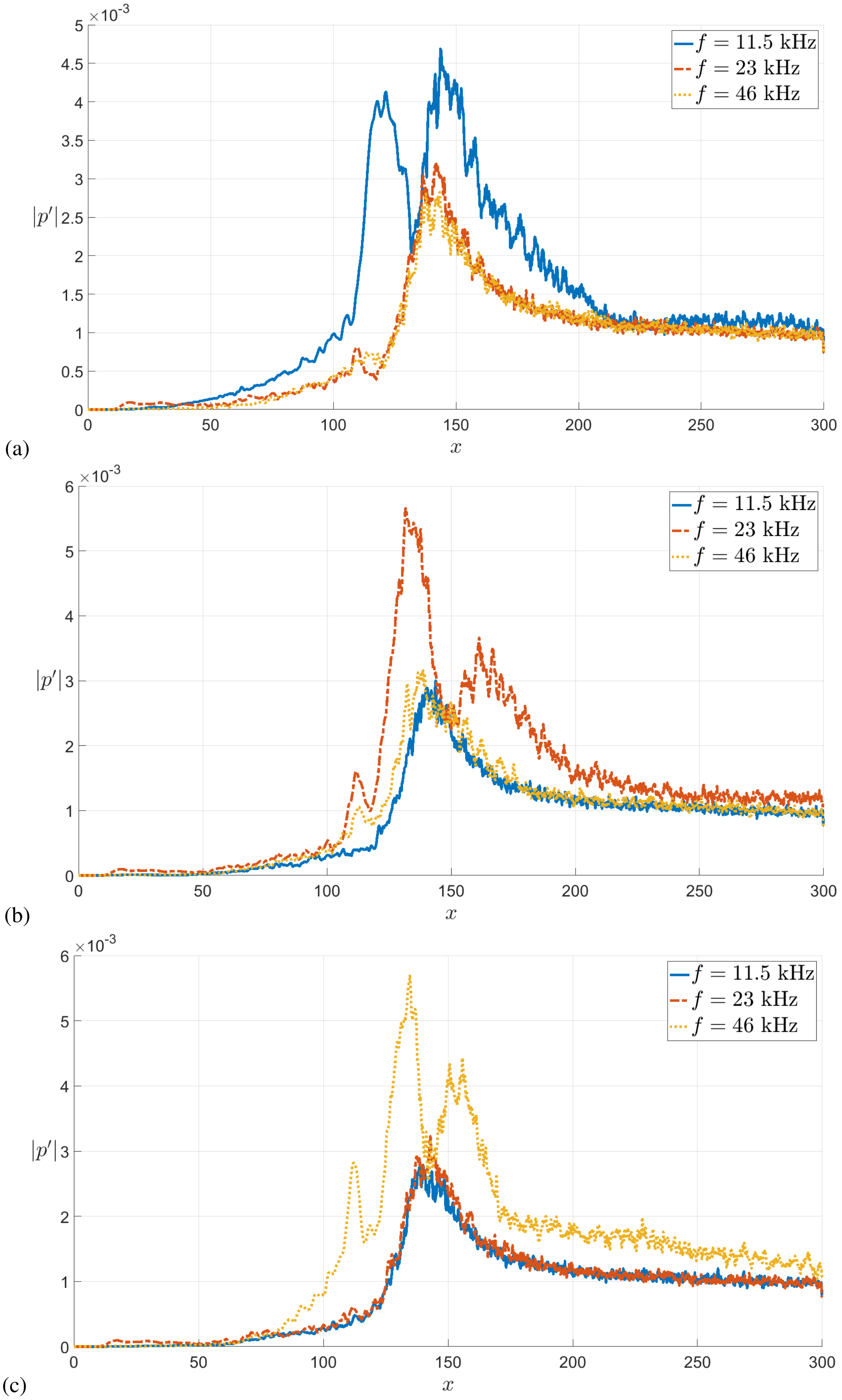

Fig. 19 Spanwise-averaged absolute value of the FFT wall-pressure fluctuations at different fundamental frequencies ($A = 3$): 11.5 kHz (a), 23 kHz (b), 46 kHz (c)

In figure 20 we show the shock-oscillation amplitude effect on different disturbance modes propagating within the turbulent boundary layer. The figure shows spanwise-averaged real part of the FFT pressure fluctuations at the fundamental frequency of 23 kHz, for different spanwise wavenumbers, at different shock-oscillation amplitudes. The $\beta = 1$ and $\beta = 2$ modes refer to oblique wave modes with spanwise wavelength equal to the whole domain width and half the domain width in the spanwise direction, respectively. These are compared with the corresponding 2D mode ($\beta = 0$) for the three cases at different oscillation amplitudes. As can be seen, for all the cases the most relevant excited mode is a 2D wave mode both in the shock interaction region and in the downstream turbulent boundary layer. Oblique modes are also present, but at a significantly lower amplitude compared to the 2D mode, particularly for larger amplitudes of the shock oscillations. In the downstream turbulent flow region, the maximum amplitude of the 2D waves at the highest considered amplitude of the shock oscillations (figure 20c) is observed to be approximately double that of the corresponding waves at the lowest amplitude (figure 20a). This, in turn, results in a larger modulation effect on the local turbulent boundary layer.

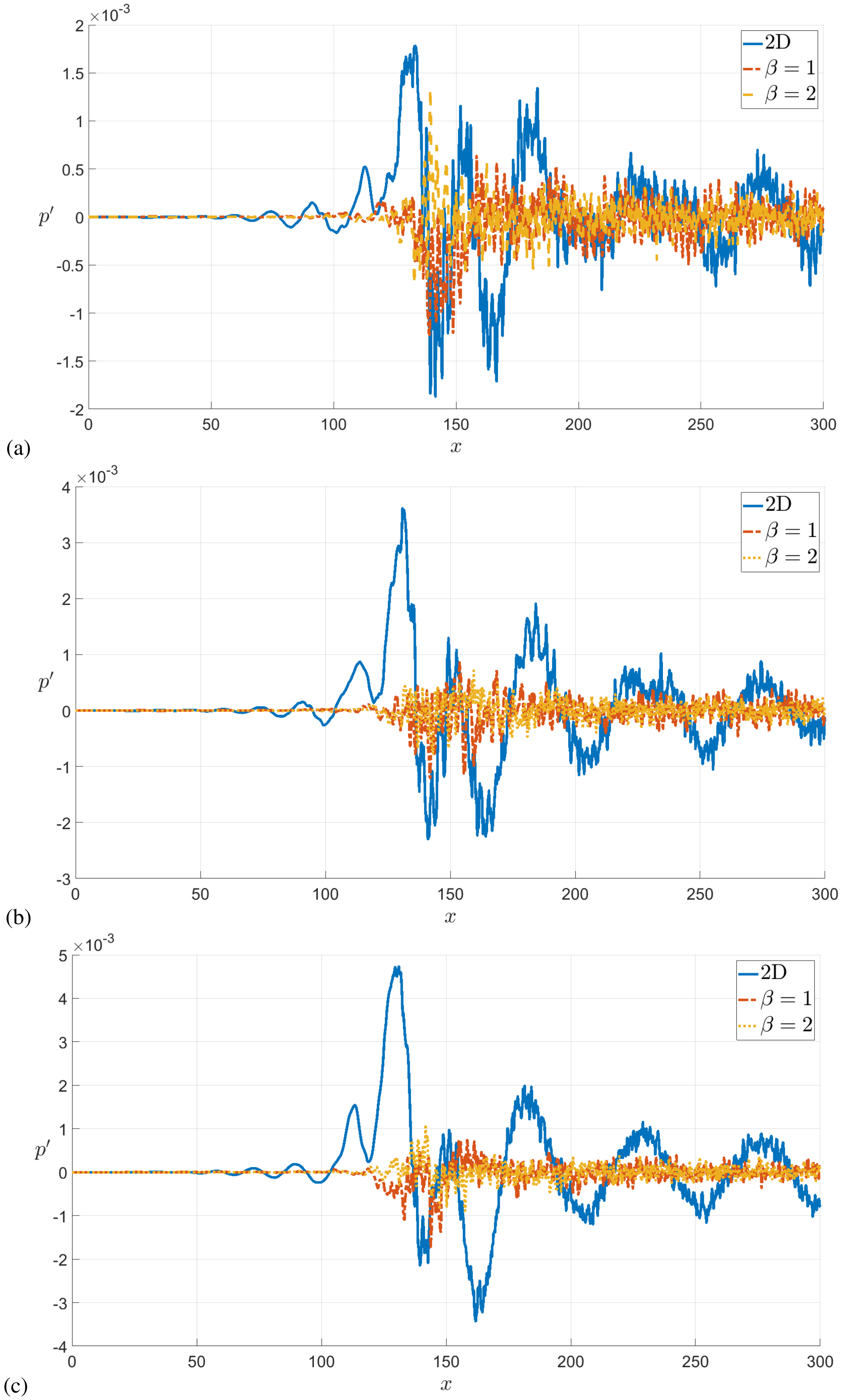

Fig. 20 Spanwise-averaged FFT wall-pressure fluctuations at different amplitudes (fundamental frequency 23 kHz): $A = 1$ (a), $A = 2$ (b), $A = 3$ (c)

Finally, figure 21 shows the effect of different fundamental frequencies of the incident shock oscillations on the FFT-response for the wall pressure fluctuations. Simulations have been performed also at the fundamental shock-oscillation frequency of 92 kHz, which is shown here for comparison with the three reference frequencies so far considered. The corresponding wave patterns at 92 kHz in the shock layer and on the wall are similar to those already observed at the three discussed frequencies (11.5 kHz, 23 kHz, 46 kHz), and reveal again the already described compact 2D-wave pattern propagating at a sustained amplitude within the turbulent boundary layer. Hence, these are not shown in the present paper for brevity purposes. As can be seen in figure 21, the high frequency (92 kHz) shows a lower peak in the interaction region, compared to the lower frequencies, however its profile in the downstream region follows closely the profile of the 46 kHz frequency. This demonstrates that even the response at high frequencies near the order $O(10^2)$ kHz is characterized by waves induced by the shock oscillations and propagating with sustained amplitude in the downstream turbulent boundary layer.

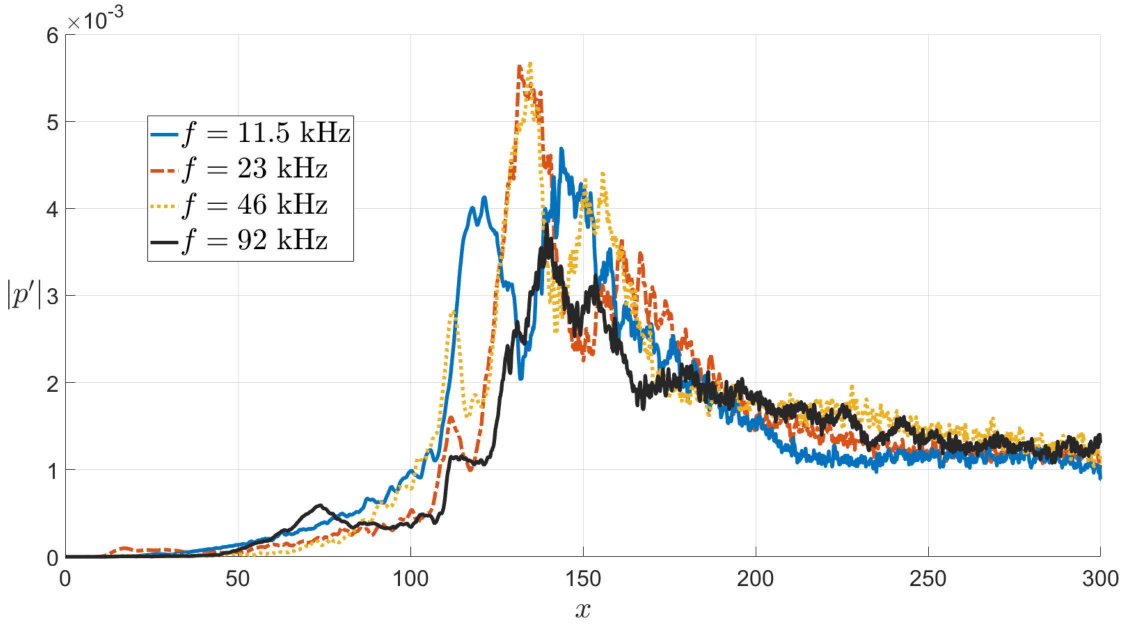

Fig. 21 Spanwise-averaged absolute value of the FFT wall-pressure fluctuations at different fundamental frequencies (A = 3)

V. Conclusion

DNS simulations have been performed for an oscillating oblique shock impinging over a transitional boundary layer in a Mach 5 flow over a flat plate, and a receptivity study has been conducted for the wave patterns in the shock layer and on the wall. The reference imposed frequency of the shock oscillations matches that obtained in a former DSMC study [37], at the considered Mach number, for the 'natural' oscillations induced by the inner-shock molecular nonequilibrium. In the present work, oscillations of the incident shock have been imposed as a time-periodic boundary condition, with the aim to mimic the effects of an oscillating shock in the same frequency range of the DSMC-predicted frequencies. A sensitivity study based on both frequency and amplitude has been carried out, in which two additional frequencies, half and double the reference DSMC-predicted frequency (23 kHz), along with three different amplitudes of the incident shock oscillations, have been considered.

Results of the pressure fluctuations within the shock layer has shown that a compact wave structure made of vertically-oriented wave fronts is generated downstream of the incident shock at the fundamental oscillation frequencies, which, after interacting with a complex wave system downstream of the separation shock, is efficiently transmitted through the reattachment shock and propagate downstream imposing an external forcing on the local turbulent boundary layer. Weaker amplitudes are observed, in contrast, for the response at frequencies different to the fundamental frequency, whose wave patterns appear, in general, more comparable with those without oscillations of the incident shock, however showing some higher-frequency nonlinearities and some pronounced unsteadiness downstream of the separation shock.

Analysis of the response on the surface has shown that the downstream turbulent boundary layer is highly affected by the post-shock wave system transmitted through the reattachment shock at the fundamental oscillation frequencies. In particular, it is found that a compact system of 2D wave fronts induced by the shock oscillations is released downstream of the reattachment shock. These amplified waves propagate up to long distances with a sustained amplitude downstream of the reattachment shock, modulating the local turbulent boundary layer. This previously unknown generation mechanism of the system of 2D planar waves within the turbulent boundary layer is altogether absent when no oscillations are imposed on the impinging shock. Consistently, an analysis of the FFT wave modes has shown the 2D wave mode as the most excited mode induced by the shock oscillations. Whereas, oblique $\beta = 1$ and $\beta = 2$ modes, although present in the downstream turbulent boundary layer, have a significantly lower amplitude. Increasing amplitudes of the shock oscillations are seen, as expected, to produce a higher amplification of the 2D waves transmitted within the downstream turbulent boundary layer, with doubled disturbance amplitude in the downstream region, compared to the lowest shock-oscillation amplitude case.

Increasing shock-oscillation frequencies within the DSMC-predicted frequency range (11.5 kHz - 46 kHz) are seen to promote a higher amplification of the 2D waves, with larger amplitudes maintained up to longer distances downstream of the reattachment shock, compared to lower frequencies. The frequency of 46 kHz of the incident shock oscillations produces a wave system with amplitude larger by 50 % than the disturbances observed in the no-oscillation case and for the subharmonic frequencies, near 3/4 of the computational domain length, and 30 % higher by the end of the computational domain. An additional analysis at a larger frequency (92 kHz) has shown a similar disturbance profile to that for the 46 kHz frequency in the downstream turbulent boundary layer, proving that the wave transmission mechanism from the incident to the reattachment shock efficiently promotes wave structures with sustained amplitude propagating within the turbulent boundary layer.

The present findings suggest that further investigation is necessary to shed light on the complex mechanism correlating dynamics of oscillating incident shocks and the induced boundary-layer instabilities, potentially exploring different frequency ranges and amplitudes of the shock oscillations, which in turn can have important implications on the aerodynamic and propulsive performance of hypersonic vehicles.

Acknowledgements

The research conducted in this paper is supported by the Office of Naval Research under the grant No. N000141202195 titled "Multiscale modelling of unsteady shock-boundary layer hypersonic flow instabilities" with Dr E. Marineau as the Program Officer. The present work has been carried out in the scope of the NATO AVT 346 "Hypersonic Boundary-Layer Transition on Complex Geometries" Task Force, chaired by Prof. Steven Schneider (Purdue University) and Dr. Stefan Hein (German Aerospace Centre - DLR). Computer time on the UK National Supercomputing Service ARCHER 2 has been provided by the UK Turbulence Consortium (UKTC), under EPSRC (Engineering and Physical Sciences Research Council) grant no. EP/D44073/1, EP/G06958/1.

References

[1] Kiriakos, R.M., Pournadali Khamseh, A., Gianoukakis, G. and DeMauro, E.P., 2022. PIV Investigation of the Effects of Shock Generator Wedge Angle and Trailing-Edge Expansion Waves on Impinging Shock/Turbulent Boundary Layer Interactions over a Cylinder. AIAA 2022-1328 Paper. https://doi.org/10.2514/6.2022-1328

[2] Chang, E.W.K., Chan, W.Y., McIntyre, T.J. and Veeraragavan, A., 2022. Hypersonic shock impingement studies on a flat plate: flow separation of laminar boundary layers. Journal of Fluid Mechanics, 951, p.A19. https://doi.org/10.1017/jfm.2022.827

[3] Hakkinen, R.J., Greber, I., Trilling, L. and Abarbanel, S.S., 1959. The interaction of an oblique shock wave with a laminar boundary layer. No. NASA-MEMO-2-18-59W.

[4] Katzer, E., 1989. On the lengthscales of laminar shock/boundary-layer interaction. Journal of Fluid Mechanics, 206, pp.477-496. https://doi.org/10.1017/S0022112089002375

[5] Lusher, D.J. and Sandham, N.D., 2020. The effect of flow confinement on laminar shock-wave/boundary-layer interactions. Journal of Fluid Mechanics, 897, p.A18. https://doi.org/10.1017/jfm.2020.354

[6] Babinsky, H. and Harvey, J.K. eds., 2011. Shock wave-boundary-layer interactions (Vol. 32). Cambridge University Press.

[7] Sivasubramanian, J. and Fasel, H.F., 2015. Numerical investigation of shock-induced laminar separation bubble in a Mach 2 boundary layer. AIAA 2015-2641 Paper. https://doi.org/10.2514/6.2015-2641

[8] Sansica, A., Sandham, N. and Hu, Z., 2013. Stability and unsteadiness in a 2D laminar shock-induced separation bubble. AIAA 2013-2982 Paper. https://doi.org/10.2514/6.2013-2982

[9] Dwivedi, A., Nichols, J.W., Jovanovic, M.R. and Candler, G.V., 2017. Optimal spatial growth of streaks in oblique shock/boundary layer interaction. AIAA 2017-4163 Paper. https://doi.org/10.2514/6.2017-4163

[10] Sandham, N.D., Schülein, E., Wagner, A., Willems, S. and Steelant, J., 2014. Transitional shock-wave/boundary-layer interactions in hypersonic flow. Journal of Fluid Mechanics, 752, pp.349-382.

[11] Saric, W., Reed, H., and Kerschen, E. *Boundary-layer receptivity to freestream disturbances*, Annual Review of Fluid Mechanics 34, 2002. https://doi.org/10.1146/annurev.fluid.34.082701.161921

[12] Fedorov, A. V., and Khokhlov, A. P. *Prehistory of Instability in a Hypersonic Boundary Layer*, Theoretical and Computational Fluid Dynamics 14 (6), 2001. https://doi.org/10.1007/s001620100038

[13] Fedorov, A. V. *Transition and Stability of High-Speed Boundary Layers*, Annual Review of Fluid Mechanics 43 (1), 2011. https://doi.org/10.1146/annurev-fluid-122109-160750

[14] Zhong, X., and Wang, X. *Direct Numerical Simulation on the Receptivity, Instability, and Transition of Hypersonic Boundary Layers*, Annual Review of Fluid Mechanics 44 (1), 2012. https://doi.org/10.1146/annurev-fluid-120710-101208

[15] Zhong, X., and Ma, Y. *Boundary-layer receptivity of Mach 7.99 flow over a blunt cone to free-stream acoustic waves*, Journal of Fluid Mechanics, 556, 2006. https://doi.org/10.1017/S0022112006009293

[16] Ma, Y., and Zhong, X. *Receptivity of a supersonic boundary layer over a flat plate, Part 3: Effects of different types of free-stream disturbances*, Journal of Fluid Mechanics 532, 2005. https://doi.org/10.1017/S0022112005003836

[17] Balakumar, P. *Receptivity of a supersonic boundary layer to acoustic disturbances*, AIAA Journal 47 (5), 2009, pp. 1069-1078. http://dx.doi.org/10.2514/1.33395

[18] Malik, M. R., and Balakumar, P. *Acoustic receptivity of Mach 4.5 boundary layer with leading-edge bluntness*, Theoretical and Computational Fluid Dynamics, 21 (5), 2007, pp. 323-342. https://doi.org/10.1007/s00162-007-0050-5

[19] Kara, K., Balakumar, P., and Kandil, O. A. *Receptivity of Hypersonic Boundary Layers Due to Acoustic Disturbances over Blunt Cone*, AIAA 2007-945 Paper. https://doi.org/10.2514/6.2007-945

[20] Egorov, I. V., Sudakov, V. G., and Fedorov, A. V. *Numerical modeling of the receptivity of a supersonic boundary layer to acoustic disturbances*, Fluid Dynamics 41 (1), 2006. https://doi.org/10.1007/s10697-006-0020-4

[21] Cerminara, A., and Sandham, N. *Boundary-layer receptivity and breakdown in hypersonic flow over a swept blunt wedge with three-dimensional freestream acoustic disturbances*, AIAA 2016-4247 Paper. https://doi.org/10.2514/6.2016-4247

[22] Cerminara, A. and Sandham, N.D., 2017. *Acoustic leading-edge receptivity for supersonic/hypersonic flows over a blunt wedge*. AIAA Journal, 55(12), pp.4234-4244. https://doi.org/10.2514/1.J055749

[23] Pasquariello, V., Hickel, S. and Adams, N.A., 2017. *Unsteady effects of strong shock-wave/boundary-layer interaction at high Reynolds number*. Journal of Fluid Mechanics, 823, pp.617-657. https://doi.org/10.1017/jfm.2017.308

[24] Andreopoulos, J. and Muck, K., 1987. *Some new aspects of the shock-wave/boundary-layer interaction in compression-ramp flows*. Journal of Fluid Mechanics, 180, pp.405-428. https://doi.org/10.1017/S0022112087001873

[25] Adams, N.A., 2000. *Direct simulation of the turbulent boundary layer along a compression ramp at M=3 and* Re_θ*= 1685*. Journal of Fluid Mechanics, 420, pp.47-83. https://doi.org/10.1017/S0022112000001257

[26] Piponniau, S., Dussauge, J.P., Debieve, J.F. and Dupont, P., 2009. A simple model for low-frequency unsteadiness in shock-induced separation. Journal of Fluid Mechanics, 629, pp.87-108. https://doi.org/10.1017/S0022112009006417

[27] Wu, M. and Martin, M.P., 2008. Analysis of shock motion in shockwave and turbulent boundary layer interaction using direct numerical simulation data. Journal of Fluid Mechanics, 594, pp.71-83. https://doi.org/10.1017/S0022112007009044

[28] Pirozzoli, S. and Grasso, F., 2006. *Direct numerical simulation of impinging shock wave/turbulent boundary layer interaction at M= 2.25*. Physics of fluids, 18(6). https://doi.org/10.1063/1.2216989

[29] Touber, E. and Sandham, N.D., 2009. *Large-eddy simulation of low-frequency unsteadiness in a turbulent shock-induced separation bubble*. Theoretical and computational fluid dynamics, 23(2), pp.79-107. https://doi.org/10.1007/s00162-009-0103-z

[30] Willems, S., Gülhan, A. and Esser, B., 2013. Shock induced fluid-structure interaction on a flexible wall in supersonic turbulent flow. Progress in Flight Physics, 5, pp.285-308. https://doi.org/10.1051/eucass/201305285

[31] Daub, D., Willems, S. and Gülhan, A., 2016. Experiments on the interaction of a fast-moving shock with an elastic panel. AIAA Journal, 54(2), pp.670-678. https://doi.org/10.2514/1.J054233

[32] Currao, G.M., Neely, A.J., Kennell, C.M., Gai, S.L. and Buttsworth, D.R., 2019. Hypersonic fluid–structure interaction on a cantilevered plate with shock impingement. AIAA journal, 57(11), pp.4819-4834. https://doi.org/10.2514/1.J058375

[33] Miller, B., Crowell, A. and McNamara, J., 2012. Modeling and analysis of shock impingements on thermo-mechanically compliant surface panels. In 53rd AIAA/ASME/ASCE/AHS/ASC Structures, Structural Dynamics and Materials Conference 20th AIAA/ASME/AHS Adaptive Structures Conference 14th AIAA (p. 1548). https://doi.org/10.2514/6.2012-1548

[34] Currao, G. M., McQuellin, L. P., Neely, A. J., Gai, S. L., O'Byrne, S., Zander, Buttsworth, D. R., McNamara, J. J., and Jahn, I. (2021). Hypersonic oscillating shock-wave/boundary-layer interaction on a flat plate. AIAA journal, 59(3), pp. 940-959. https://doi.org/10.2514/1.J059590

[35] Wagner, A., Schülein, E., Petervari, R., Hannemann, K., Ali, S.R., Cerminara, A. and Sandham, N.D., 2018. Combined free-stream disturbance measurements and receptivity studies in hypersonic wind tunnels by means of a slender wedge probe and direct numerical simulation. Journal of Fluid Mechanics, 842, pp.495-531. https://doi.org/10.1017/jfm.2018.132

[36] Sawant, S.S., Theofilis, V. and Levin, D.A., 2022. *On the synchronisation of three-dimensional shock layer and laminar separation bubble instabilities in hypersonic flow over a double wedge*. Journal of Fluid Mechanics, 941. https://doi.org/10.1017/jfm.2022.276

[37] Sawant, S.S., Levin, D.A. and Theofilis, V., 2021. *Analytical prediction of low-frequency fluctuations inside a one-dimensional shock*. Theoretical and Computational Fluid Dynamics, pp.1-16. https://doi.org/10.1007/s00162-021-00589-5

[38] Sawant, S.S., Levin, D.A. and Theofilis, V., 2021. *A kinetic approach to studying low-frequency molecular fluctuations in a one-dimensional shock*. Physics of Fluids, 33(10), p.104106. https://doi.org/10.1063/5.0065971

[39] Fedorov, A. and Tumin, A., 2017. *Receptivity of high-speed boundary layers to kinetic fluctuations*. AIAA Journal, 55(7), pp.2335-2348. https://doi.org/10.2514/1.J055326

[40] Tumuklu, O., Theofilis, V. and Levin, D.A., 2018. *On the unsteadiness of shock–laminar boundary layer interactions of hypersonic flows over a double cone*. Physics of Fluids, 30(10), p.106111. https://doi.org/10.1063/1.5047791

[41] Karpuzcu, I.T, Senkardesler, M., and Levin, D.A., 2025. *On Flow Unsteadiness in Strongly Separated High-Speed Ramp Flows using Kinetic and Data Driven Methods*. Physics of Fluids, 37(9). https://doi.org/10.1063/5.0281770

[42] Cerminara, A. and Sandham, N., 2020. *Transition mechanisms in cross-flow-dominated hypersonic flows with free-stream acoustic noise*. Journal of Fluid Mechanics, 896. https://doi.org/10.1017/jfm.2020.346

[43] Klothakis, A., Quintanilha Jr, H., Sawant, S.S., Protopapadakis, E., Theofilis, V. and Levin, D.A. *Linear stability analysis of hypersonic boundary layers computed by a kinetic approach: a semi-infinite flat plate at* $4.5 \leq M_\infty \leq 9$. Theor. Comput. Fluid Dyn. 36, 117–139 (2022). https://doi.org/10.1007/s00162-021-00601-y

[44] Cerminara, A., Levin, D.A. and Theofilis, V., 2023. Shock receptivity: characteristics of shock oscillation modes and induced boundary-layer disturbances. AIAA 2023-0871 Paper. https://doi.org/10.2514/6.2023-0871

[45] Yee, H. C., Sandham, N. D., and Djomehri, M. J. *Low-dissipative high-order shock-capturing methods using characteristic-based filters*, Journal of Computational Physics 150 (1), pp. 199-238, 1999. https://doi.org/10.1006/jcph.1998.6177

[46] De Tullio, N., Paredes, P., Sandham, N. D., and Theofilis, V. *Laminar-turbulent transition induced by a discrete roughness element in a supersonic boundary layer*, Journal of Fluid Mechanics 735, pp. 613-646, 2013. https://doi.org/10.1017/jfm.2013.520

[47] Cerminara, A., Deiterding, R. and Sandham, N., 2020. *A mesoscopic modelling approach for direct numerical simulations of transition to turbulence in hypersonic flow with transpiration cooling*. International Journal of Heat and Fluid Flow, 86, p.108732. https://doi.org/10.1016/j.ijheatfluidflow.2020.108732

[48] Cerminara, A., Hermann, T., Ifti, H.S., Deiterding, R., Sandham, N. and McGilvray, M., 2021. *Influence of instability modes on cooling performance in hypersonic boundary layer with slot injection*. Aerospace Science and Technology, 109, p.106409. https://doi.org/10.1016/j.ast.2020.106409

[49] Van Driest, E.R., 1956. The problem of aerodynamic heating. Los Angeles: Institute of the Aeronautical Sciences.

[50] Anderson, J.D., 2006. Hypersonic and High-Temperature Gas Dynamics. 2nd edn, AIAA Education Series (2006)

[51] Cerminara, A., 2023. *Turbulence effect on transpiration cooling effectiveness over a flat plate in hypersonic flow and sensitivity to injection parameters*. Flow, Turbulence and Combustion, 110(4), pp.945-968. https://doi.org/10.1007/s10494-023-00403-8

[52] Coleman, G.N. and Sandberg, R.D., 2010. *A primer on direct numerical simulation of turbulence-methods, procedures and guidelines*. Technical Report AFM-09/01a, University of Southampton.

[53] Yang, X.I., Hong, J., Lee, M. and Huang, X.L., 2021. *Grid resolution requirement for resolving rare and high intensity wall-shear stress events in direct numerical simulations*. Physical Review Fluids, 6(5), p.054603. https://doi.org/10.1103/PhysRevFluids.6.054603

[54] Wenzel, C., Selent, B., Kloker, M. and Rist, U., 2018. DNS of compressible turbulent boundary layers and assessment of data/scaling-law quality. Journal of Fluid Mechanics, 842, pp.428-468. https://doi.org/10.1017/jfm.2018.179

[55] Duan, L., Beekman, I. and Martin, M.P., 2011. Direct numerical simulation of hypersonic turbulent boundary layers. Part 3. Effect of Mach number. Journal of Fluid Mechanics, 672, pp.245-267. https://doi.org/10.1017/S0022112010005902